Chemical Engineering Journal 542 (2026) 177824

Contents lists available at ScienceDirect

Chemical Engineering Journal

journal homepage: www.elsevier.com/locate/cej

Sustainable one-step synthesis of rare-earth-doped carbon quantum dots from agro-industrial and electronic waste precursors☆

Konrad Wojtaszek [a], Tomasz Michałek [a], Katarzyna Skibińska [a], Adrianna Pach [a], Krzysztof Pitala [b], Krzysztof Mech [c], Hossain Aghajani [d,a], Edit Csapó [e,f], Robert P. Socha [g,h], Marek Wojnicki [a,*]

[a] AGH University of Krakow, Faculty of Non-Ferrous-Metals, al. Mickiewicza 30, 30-059, Krakow, Poland
[b] National Synchrotron Radiation Centre SOLARIS, Jagiellonian University, Czerwone Maki 98, 30-392, Kraków, Poland
[c] AGH University of Krakow, Academic Centre of Materials and Technology, al. Mickiewicza 30, 30-059, Krakow, Poland
[d] School of Metallurgy & Materials Engineering, Iran University of Science & Technology, Narmak, Tehran, Iran
[e] MTA-SZTE Lendület "Momentum" Noble Metal Nanostructures Research Group, University of Szeged, Rerrich B. sqr. 1, H-6720, Szeged, Hungary
[f] Interdisciplinary Excellence Center, Department of Physical Chemistry and Materials Science, University of Szeged, Rerrich B. sqr. 1, H-6720, Szeged, Hungary
[g] Jerzy Haber Institute of Catalysis and Surface Chemistry, Polish Academy of Sciences, Niezapominajek 8, Kraków, 30-239, Poland
[h] CBRTP SA Research and Development Center of Technology for Industry, Zygmunta Modzelewskiego 77, 02-679, Warszawa, Poland

ARTICLE INFO

Keywords:
Carbon quantum dots
Rare-earth doping
Green synthesis
Sustainable development
Waste valorization
EXAFS

ABSTRACT

The key scientific question addressed in this study is whether an agro-industrial biomass precursor and a real electronic-waste-derived rare-earth source can be coupled in a single hydrothermal process to produce carbon quantum dots (CQDs) with preserved carbon-core structure and tunable optical/magnetic properties.

A one-step, waste-based hydrothermal synthesis of CQDs directly from cherry-seed biomass and spent fluorescent-lamp phosphor powder is reported, achieving in situ modification with rare-earth elements (REEs). The method simultaneously enables carbonization, nanoparticle formation, and REE coordination without multi-stage post-functionalization Structural and morphological characterization by HR-TEM reveals small graphitic domains (~2–4 nm) preserved upon REE modification. XPS and EDX provide evidence for surface-associated REE species, particularly Dy- and Ho-containing environments, coordinated to oxygen- and nitrogen-containing functional groups. Carbon K-edge XAS analysis indicates that the CQDs preserve a stable sp^2-dominated carbon framework, with structural features governed primarily by surface-localized oxygen-containing functional groups. FT-IR and UV–Vis spectroscopy indicate changes in the surface ligand environment and the emergence of subtle metal-related electronic states. Photoluminescence studies demonstrate tunable emission: undoped CQDs blue-shift upon dialysis ($\lambda_{em} \approx 440$ nm), whereas REE-doped show red-shifted emission ($\lambda_{em} \approx 500$ nm) and enhanced radiative pathways via metal-ligand charge transfer. Magnetic measurements reveal a three-fold increase in paramagnetic responsiveness in REE-doped CQDs compared to undoped counterparts. These findings establish a sustainable, facile route to multifunctional CQDs with combined optical and magnetic properties, highlighting their potential relevance for future imaging-related applications, provided that cytotoxicity, colloidal stability in biological media, and REE ion-leakage are systematically evaluated.

Abbreviations

CQDs	Carbon Quantum Dots
REE	Rare-Earth Elements
FT-IR	Fourier Transform Infrared Spectroscopy
XRD	X-Ray Diffraction
HR-TEM	High-Resolution Transmission Electron Microscopy
MP-AES	Microwave Plasma-Atomic Emission Spectroscopy
UV–Vis	Ultraviolet–Visible Spectroscopy
Ln–O	Lanthanide–Oxygen bond
λ_{em}	Emission wavelength
XPS	X-ray Photoelectron Spectroscopy

☆ This article is part of a Special issue entitled: 'Carbon Waste Valorisation' published in Chemical Engineering Journal.

* Corresponding author.
E-mail address: marekw@agh.edu.pl (M. Wojnicki).

https://doi.org/10.1016/j.cej.2026.177824
Received 18 February 2026; Received in revised form 4 May 2026; Accepted 28 May 2026
Available online 28 May 2026

EXAFS	Extended X-ray Absorption Fine Structure (measured at a synchrotron facility)
LOD	Limit of Detection
S/N	Signal-to-Noise ratio
MRI	Magnetic Resonance Imaging
TEY	Total Electron Yield
FWHM	Full Width at Half Maximum
π–π^*	pi to pi star transition
n–π^*	n to pi star transition
Ln^{3+}	Trivalent lanthanide ion

1. Introduction

Electronic waste (e-waste) has emerged as a significant environmental concern in recent decades, driven by the rapid proliferation of electronic devices and their relatively short life spans [1,2]. Among the various categories of e-waste, spent fluorescent lamp phosphor powder (SFLs) present unique challenges due to their complex composition and hazardous constituents, notably mercury [3]. Improper disposal of SFLs can lead to mercury release, posing serious environmental and health risks [4,5]. Despite existing recycling initiatives, the intricate makeup of these lamps complicates efficient material recovery, particularly for valuable rare earth elements contained within the phosphor powders [6]. Moreover, global projections indicate that e-waste volumes are expected to surpass 70 million metric tons by 2030, underscoring the urgency of developing scalable, sustainable recycling strategies [7]. Consequently, developing methodologies that facilitate the direct conversion of such waste into valuable materials is of paramount importance, aligning with the principles of a circular economy aimed at minimizing waste and maximizing resource utilization [8].

Carbon quantum dots (CQDs) have garnered considerable attention owing to their exceptional photoluminescent properties, excellent biocompatibility [9], chemical stability [10], and ease of surface functionalization [11], opening doors for diverse applications ranging from bioimaging and sensing to optoelectronics [12]. The synthesis of CQDs can be broadly categorized into two main approaches: traditional “gray” synthesis, which typically employs hazardous chemical reagents and often involves harsh reaction conditions, and “green” synthesis, which utilizes biomass or bio-waste as environmentally benign carbon sources [13]. While the former can offer greater control over the physicochemical properties of the resulting CQDs, it often involves toxic precursors and energy-intensive processes, raising environmental concerns. In contrast, green synthesis aligns strongly with the principles of sustainable development, offering an eco-friendly and cost-effective alternative that repurposes abundant agricultural and industrial waste materials, thereby minimizing environmental impact [14].

Green synthesis approaches often rely on regionally abundant agricultural residues, ensuring both sustainability and economic viability [15]. In this context, identifying suitable biomass sources at a local scale becomes essential for practical implementation. Poland stands as one of Europe's leading producers of cherries, with production figures reaching over 200,000 metric tons in recent years [16]. This substantial yield results in significant quantities of cherry seeds as by-products, which are often underutilized [17]. Given the environmental impact associated with long-distance transportation of raw materials, as highlighted by life cycle assessment (LCA) studies, it is advantageous to exploit locally available resources for material synthesis [18]. Utilizing cherry seeds, an abundant and renewable local biomass, as a carbon source for CQD synthesis not only adds value to this agricultural waste but also minimizes the carbon footprint associated with material transportation.

The biomass precursor should not be regarded only as a carbon source, because its chemical structure can influence the surface chemistry and performance of the resulting CQDs. Cherry-seed biomass is expected to contain lignocellulosic and polyphenolic fractions bearing hydroxyl, ether, carbonyl, and carboxyl-containing motifs. During hydrothermal carbonization, these structural units can undergo dehydration, fragmentation, aromatization, and partial oxidation, producing small sp^2-rich carbon domains decorated with oxygen-containing surface groups. These groups are important for aqueous dispersibility, pH-dependent photoluminescence, surface-state emission, and coordination of metal ions.

In the present study, the exact quantitative content of individual –OH, –COOH, and related groups in the raw cherry-seed biomass was not determined. Therefore, we do not make a quantitative claim regarding the precursor composition. However, the FT-IR and XPS results obtained for the final CQDs confirm the presence of surface O—H, C—O, C═O, carboxylate-related, and N/O-containing environments. These functional groups provide chemically active sites that can interact with REE ions released from spent fluorescent-lamp phosphor powder. Thus, the biomass-derived surface chemistry is directly relevant to the observed photoluminescence behavior, colloidal properties, and REE coordination. This interpretation is also consistent with our recent systematic work on carbon dots, where precursor type, synthesis conditions, surface chemistry, optical properties, and cytotoxicity were discussed as interconnected factors governing CQD performance [19].

Incorporating REEs into CQDs can endow the resulting nanomaterials with combined optical and magnetic functionalities, including tunable photoluminescence and enhanced magnetic response [20]. Such multifunctional CQDs are frequently discussed in the context of multimodal imaging concepts and other advanced functional applications [21,22]. However, when REE-modified CQDs are prepared from real waste-derived REE sources, biomedical applicability should be regarded as a long-term perspective rather than an immediate claim. Spent fluorescent-lamp phosphor powder is chemically complex and may introduce residual impurities, competing metal ions, and loosely bound REE species. Therefore, before any bioimaging or biomedical use can be considered, cytotoxicity, colloidal stability in biologically relevant media, impurity transfer, and possible REE ion leakage must be systematically evaluated. In the present work, the optical and magnetic responses of the obtained REE-modified CQDs are therefore treated primarily as materials-level functionalities, while biological validation is identified as a necessary future step.

This study focuses on the development of a one-step, sustainable synthesis method for REE-doped CQDs using cherry seeds as the carbon source and phosphor powders extracted from spent fluorescent lamp phosphor powder as the REE source. This approach not only addresses the pressing issue of e-waste management but also contributes to the advancement of green nanotechnology by transforming waste materials into high-value, multifunctional nanomaterials with potential biomedical applications.

2. Experimental

Schematic representation of the synthesis methodology for rare earth element (REE)-doped CQDs is shown in Fig. 1. Cherry seeds were used as the carbon source for CQD synthesis. Prior to the experimental procedure, the cherry seeds were thoroughly dried and subsequently ground into a fine powder to increase the surface area and improve reactivity.

A similar preparation process was applied to the spent fluorescent lamp phosphor powder, which served as the source of rare earth elements. The lamps were first carefully disassembled, and the phosphor-containing residues were collected and milled to obtain a fine particulate powder.

In the next step, both the cherry pit powder and the powdered fluorescent lamp residue were introduced into a Teflon-lined autoclave reactor. A solvent mixture consisting of hydrochloric acid (HCl) and ethanol was then added to the reactor vessel. Hydrochloric acid was used to enhance the leaching efficiency of REEs from the spent lamp materials, while ethanol facilitated the extraction of organic compounds from the cherry pit biomass.

The synthesis was carried out under high-pressure and high-

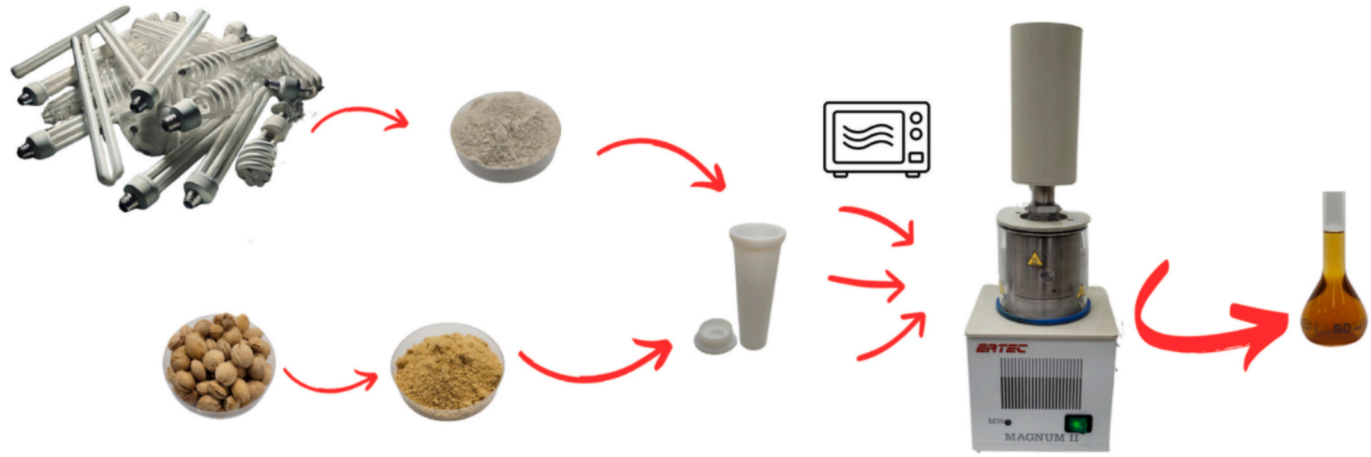

Fig. 1. Methodology of REE-doped CQDs synthesis.

temperature conditions using a microwave-assisted hydrothermal process.

Fig. 2 presents a representative profile of the synthesis process for REE-doped CQDs. The x-axis represents time, whereas the y-axis shows normalized process parameters, including pressure, temperature, microwave power, and reflected power.

The microwave generator used in this setup operates in a pulsed on-off mode with a fixed output power of 300 W. Due to the nature of the heating process, the temperature sensor is not placed directly inside the reaction vessel but positioned adjacent to it. As a result, the recorded temperature values exhibit a notable delay compared to the actual temperature inside the reactor. In contrast, readings of pressure, microwave power, and reflected power are acquired in real time.

For safety and process control purposes, both upper and lower threshold limits were established for temperature and pressure. The process control software is designed to ensure that none of the maximum values are exceeded, while at least one of the minimum values (either temperature or pressure) is reliably reached during the synthesis.

After the reaction is complete, the system undergoes a controlled cooling phase. Only once the external temperature sensor registers a value close to 40 °C is the reactor chamber opened. At this point, the pressure vessel is safely removed from the microwave reactor for further post-synthesis processing.

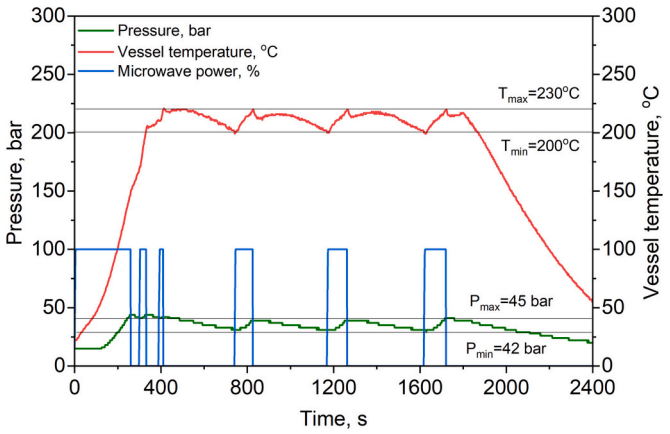

Fig. 2. Example time course of the microwave-assisted hydrothermal synthesis of REE-doped carbon quantum dots (CQDs), illustrating system parameters such as pressure, temperature, and microwave power throughout the reaction.

2.1. Materials and precursor preparation

Carbon quantum dots (CQDs) were synthesized using a sustainable approach with cherry seeds as the green carbon source. Initially, cherry seeds were collected, thoroughly cleaned, and dried. The dried seeds were then ground using a laboratory roller-ring mill (EKO–LAB, Brzesko, Poland) for 30 s to obtain a fine and homogeneous powder.

To minimize moisture-related variability in the subsequent hydrothermal synthesis, the moisture content of the milled cherry seed powder was determined using an OHAUS MB62 moisture analyzer. Based on repeated measurements, the average moisture content was determined to be 4.03 ± 0.13 wt%, with the uncertainty expressed as the standard deviation.

The elemental carbon and sulfur contents of the cherry-seed precursor were determined using a LECO CS 600 carbon/sulfur analyzer. The measurement was performed in triplicate. The cherry-seed powder contained 55.73 ± 1.73 wt% carbon and 0.94 ± 0.10 wt% sulfur. This analysis was used as a basic elemental characterization of the biomass precursor prior to CQD synthesis. However, this elemental analysis does not quantify individual –OH or –COOH groups; therefore, the discussion of surface functionalities is based primarily on the FT-IR and XPS results obtained for the final CQDs.

2.2. Leaching and elemental characterization of spent fluorescent-lamp phosphor powder

As a source of REE metal ions for doping the CQDs, spent fluorescent tubes were employed. The tubes were mechanically ground to achieve a fine powder, ensuring a consistent starting material for the REE extraction process. To quantify the REE content present in the fluorescent tube material, leaching methods were implemented, as well as XRF of dry powder. Microwave Autoclave Leaching: A 0.1010 g sample was digested in 50 cm^3 of 1 M HCl under microwave-assisted high-pressure conditions. Classical "Reverse Aqua Regia" Leaching: A separate 0.1124 g sample was treated at ambient temperature in 100 cm^3 of a mixed acid solution containing 6 M HNO_3 (65%, Supplier: PureLand, p.a.) and 1 M HCl. Following leaching, the obtained solutions were filtered to remove any residual solid particles and then analyzed using MP-AES 4200 Agilent.

2.3. One-step microwave-assisted hydrothermal synthesis of CQDs and REE-modified CQDs

The synthesis was carried out in a high-temperature, high-pressure reactor (Ertec, model Magnum II).

For the synthesis of REE-modified CQDs, 0.500 g of ground cherry-

seed powder and 0.065 g of spent fluorescent-lamp phosphor powder were introduced into the Teflon-lined reactor. This ratio was selected as a proof-of-concept compromise between providing an excess of biomass-derived carbon precursor for CQD formation and introducing a sufficient amount of phosphor powder to release REE species capable of modifying the CQD surface. The ratio was not optimized for maximum CQD yield or maximum REE incorporation, which is identified as a subject for future process optimization.

The HCl/ethanol ratio was 24:1 (*v*/v). This solvent composition was selected to combine two functions in a single reaction medium. Hydrochloric acid promotes the release of REE species from the spent fluorescent-lamp phosphor powder, whereas the small addition of ethanol improves wetting of the biomass and extraction of soluble organic compounds from the cherry-seed precursor. The ethanol fraction was kept low to avoid excessive organic-solvent content under hydrothermal conditions while still assisting the transfer of biomass-derived organic species into the liquid phase, where carbonization and CQD nucleation can occur more effectively.

In a typical reaction, the ground cherry seed powder was mixed into a solution prepared by combining 24 cm^3 of 1 M hydrochloric acid (HCl) with 1 cm^3 of ethanol (96%, Supplier: PureLand, p.a.). The 1 M HCl solution was obtained by diluting concentrated hydrochloric acid (37%, Supplier: Avantor, p.a.) with deionized water. All experiments utilized deionized water from Polwater (model DL2–100). The elevated temperature and pressure conditions were selected to promote CQD formation optimized to facilitate the formation of CQDs with enhanced luminescent properties and uniform morphology.

2.4. Purification by dialysis

Selected colloids were also prepared in a dialyzed form. Immediately after the reaction, the solution was purified via 24-h dialysis. The process utilized dialysis tubes with a regenerated cellulose membrane (Medicell International Ltd., MWCO 12–14 kDa), featuring a wall thickness of 0.03 mm, a diameter of 28.6 mm, and a length of approximately 30 cm. This procedure was used as a purification step to remove low-molecular-weight organic by-products, residual acid, salts, and free or weakly bound ionic species from the post-reaction mixture. In the case of REE-modified CQDs, dialysis can also partially remove weakly adsorbed or electrostatically associated REE ions, whereas more strongly coordinated REE species are expected to remain associated with the CQD surface. The dialysis process was repeated three times. The dialysis process was repeated three times.

2.5. Magnetic-response measurements

Magnetic properties were analyzed using a custom-built test setup [23]. The magnetic interaction was quantified as the apparent change in mass registered by the balance, which corresponds to the vertical force exerted by the magnetic field on the sample. The tested solution was placed in a quartz cuvette and positioned on an analytical balance, separated from the magnetic field by a dedicated element. A set of neodymium magnets (0.5387 T) attached to a stepper motor was gradually brought closer to the sample. The balance recorded the interaction force as an apparent mass change, which was monitored over the measurement time corresponding directly to the distance of the magnet from the sample surface. The maximum apparent mass change was observed when the magnet was positioned at 10 μm from the sample surface. The maximum apparent mass change corresponds to the sample's relative magnetic susceptibility.

2.6. FT-IR spectroscopy

FT-IR analysis was performed using a Nicolet 380 FT-IR spectrometer (Thermo Fisher Scientific) operating in transmission mode. Prior to analysis, the dried samples were homogenized with spectroscopic-grade KBr suitable for FT–IR measurements and pressed into transparent pellets. Spectra were recorded in the range of 4000–400 cm^{-1} with a spectral resolution of 4 cm^{-1}. For each sample, 100 scans were collected and averaged to improve the signal-to-noise ratio. The obtained spectra were used to identify the main surface functional groups of the CQDs and to compare vibrational features before and after REE modification.

2.7. Raman analysis

Measurements were carried out using a MonoVista CRS^3 500 Raman microscope, operating with a 532 nm laser at a power of 4.5–5.5 mW (with a neutral-density filter set to 1.5) and equipped with a 300 /mm grating. An Olympus BX53 microscope with a 100× objective lens was used for focusing. The Raman spectra were recorded over the 75–4600 cm^{-1} range, with an exposure time of 1 s and 10 accumulations per measurement. The measurements were performed at the Complementary Techniques Section of the ASTRA beamline at the SOLARIS Synchrotron (Kraków, Poland).

Samples of CQD and REE–doped CQD colloids were drop-cast onto silicon substrates coated with a 100 nm Au layer. The 100 nm gold films on silicon were prepared according to the methodology described in our previous work [24]. Briefly, the Au-coated Si substrates were used to provide a stable, conductive, and Raman-compatible surface for the deposition of the colloidal samples. After drop-casting, the samples were allowed to dry at room temperature prior to Raman measurements.

2.8. Structural and morphological characterization

HR-TEM were recorded using the FEI TECNAI TF 20 X–TWIN instrument. A drop of colloidal suspension after the dialysis process was placed onto a copper grid pre-coated with amorphous carbon film (Ultrathin Carbon Film on Lacey Carbon Support Film, 400 mesh). The samples were allowed to dry at room temperature.

To investigate the crystalline structure of the fluorescent tubes, XRD analysis was conducted using a Rigaku diffractometer (RIGAKU, Primini, Japan) with the use of a copper tube ($\lambda = 1.54059$ Å). The obtained diffraction patterns helped in confirming the structural integrity and phase composition of the analyzed materials.

2.9. Optical characterization and PL lifetime measurements

The optical properties, specifically the fluorescence emission of the synthesized CQDs, were characterized using a Horiba FluoroMax spectrophotometer. These measurements were critical for assessing the impact of REE doping on the CQDs' luminescence. Fluorescence quantum yield (QY(%)) measurements were performed using an integrating sphere (Jasco ILF-835 with 100 mm diameter). QY(%) calculation was performed using the built-in software (ABL&E JASCO SpectraManager 2.0 software) of the Jasco FP-8500 spectrofluorometer based on two recorded spectra: (1) direct excitation, where the exciting beam hits the sample directly and only diffused light excites the sample, and (2) a spectrum recorded without a sample for the measurement of scattered light. The recorded spectra were corrected using a Jasco Calibrated Light Source-WI (ESC-842) without using other references. Fluorescence (PL) lifetime studies were carried out using a Horiba DeltaFlex time-correlated single photon counting (TCSPC) device. Multiple samples were analyzed in a 10 mm quartz cuvette using a DeltaDiode pulsed laser as a light source ($\lambda = 371$ nm), and a 400 nm long pass filter was employed. All measurement data were registered using a 4 MHz repetition rate in the range of 0–200 ns, with a wide slit value of 8 nm due to the long lifetime components and relatively low quantum yields. The instrument response function (IRF) was determined with multiple settings for the correction of very short lifetimes using a standard silica dispersion provided by Horiba. The decay curves were evaluated using the EZTime program included with the equipment. The measurement data were fitted using exponential functions, and the lifetime

components were determined, while the fitting was characterized by the obtained χ^2 values.

2.10. Surface chemical analysis by XPS

The elemental composition of a representative CQD, following a modification test, was determined using X-ray Photoelectron Spectroscopy (XPS). The analysis was conducted with an ESCA/XPS photoelectron spectrometer, equipped with an SES R4000 hemispherical analyzer (Gammadata Scienta). A PREVAC RS40B1 lamp served as the source of Mg Kα radiation (1253.6 eV), operating at 180 W. The sample was prepared by being deposited onto indium, mounted on a dedicated holder, and then subjected to 3 h of initial pumping before being transferred into an ultra UHV environment for analysis. Survey spectra were acquired at 0.25 eV intervals, while detailed spectra were recorded with a finer resolution of 0.05 eV intervals. For data processing, CasaXPS 2.3.26PR1.0 software was utilized. Spectra were calibrated to the Fermi edge, and backgrounds were managed using the Shirley algorithm. Spectral lines were fitted with the Voigt function.

2.11. Soft X–ray absorption spectroscopy

Soft-X-ray measurements were carried out at the PIRX beamline of the SOLARIS National Synchrotron Radiation Centre (Krakow, Poland). For XAS, the samples were prepared by drop-casting the colloidal dispersions onto diced Si wafers (~4 × 4 mm). A ~ 5 μL aliquot of the colloid was deposited per drop and allowed to evaporate at room temperature; this deposition cycle was repeated three times to increase surface coverage. A gradual increase in the dullness of the Si surface was visible in subsequent stages of colloid deposition. The coated Si pieces were then affixed to a standard molybdenum sample holder using double-sided conductive carbon tape, which ensured reliable electrical grounding and minimized charging during acquisition. Immediately after mounting, the specimens were transferred into the analysis system and kept under ultra-high vacuum (UHV). All scans were corrected for beamline/substrate background using three reference measurements collected on a clean substrate. For each spectrum, the background signal was interpolated to the measurement grid, averaged, and scaled to the pre-edge by least-squares (α). The scaled background (α·BG) was subtracted from the raw signal prior to normalization. This step is particularly important at the C K-edge due to weak carbon contamination in the beam path and from the substrate environment.

3. Results and discussion

3.1. Analysis of rare-earth element composition in fluorescent-lamp phosphor powder

Before CQD synthesis, the spent fluorescent-lamp phosphor powder was characterized as the REE-containing precursor. Its leachability was evaluated using classical acid leaching and microwave-assisted autoclave leaching, and the resulting solutions were analyzed by MP-AES. The results obtained are presented in the table below (see Table 1).

It is worth recalling and emphasizing that the same leaching mixture was used in both cases.

Because the same leaching medium was used for both procedures, the higher REE concentrations obtained after microwave-assisted autoclave leaching indicate that elevated temperature and pressure enhance the release of REE species from the phosphor matrix.

MP-AES results are reported as concentrations, with "n.d." indicating values below the LOD; LODs for each element and the analytical wavelengths used are provided in Table 1. Where applicable, alternative emission lines were selected to minimize spectral overlap (particularly in the presence of high Y and Pr XPS-derived atomic percentages refer to the top surface (~5–10 nm) and are not directly comparable to bulk MP-AES concentrations [25].

Table 1
REEs extracted from spent fluorescent lamp phosphor powder.

Element	Classic leaching, ppm	Autoclave leaching, ppm
Lu	n.d.	n.d.
Yb	0.02 ±0.0018	n.d.
Er	0.03 ± 0.0035	0.07 ± 0.0022
Gd	3.36 ± 0.077	2.76 ± 0.08
Ho	0.02± 0.00059	n.d.
Tb	6.51 ± 0.023	7.42 ± 0.033
Dy	0.03 ± 0.00071	0.03 ± 0.000036
Sc	0.04 ± 0.0034	0.02 ± 0.00045
Y	127.59 ± 1.1	104.36 ± 0.018
Eu	7.86 ± 0.028	6.73 ± 0.017
Tm	n.d.	n.d.
Pr	208.48 ± 2.7	404.29 ± 3.4
Nd	n.d.	n.d.
Sm	n.d.	n.d.
Ce	10.98 ± 0.23	11.95 ± 0.42
La	113.51 ± 3.1	106.61 ± 1.1
Cu	0.68 ± 0.0035	0.78 ± 0.0059
Zn	0.71 ± 0.02	0.60 ± 0.003
Sr	9.03 ± 0.088	8.97 ± 0.034
Ca	333.42 ± 2.6	339.20 ± 3.4
Mg	2.71 ± 1.1E-02	4.01 ± 0.015
Ba	85.52 ± 0.7	76.10 ± 0.32
Fe	6.01 ± 0.042	5.67 ± 0.04
Al	25.27 ± 0.22	49.74 ± 0.09
Na	14.00 ± 0.46	31.31 ± 0.44
K	1.52 ± 0.0091	2.71 ± 0.016

This distinction is particularly important for CQDs, where REE species are expected to be localized mainly at the surface through coordination with oxygen- and nitrogen-containing functional groups rather than being uniformly distributed throughout a bulk crystalline phase. Consequently, MP-AES reflects the solution-accessible elemental composition after leaching/digestion, whereas XPS selectively probes surface-enriched REE species present on the dried CQD surface. These two techniques therefore provide complementary, but not directly interchangeable, information on REE incorporation.

It should also be noted that the elemental composition of the luminescent lamp residue is highly complex. In addition to a significant fraction of REEs, it also contains measurable amounts of transition metals as well as light metals. While the presence of light metals is of minor importance for the process due to their abundance and their occurrence in the organic precursor (carbon quantum dots derived from biomass such as seeds), the transition metals can play a more critical role. Specifically, their coexistence with REEs in the leachates may influence the modification pathways of CQDs, potentially leading to effects not typically observed in synthetic systems, where REE dopants are usually studied in isolation. This complexity introduces an additional degree of realism and may open opportunities for obtaining novel luminescent properties of CQDs that are difficult to reproduce in simplified laboratory conditions. At the same time, this multicomponent composition may also influence the synthesis and properties of the resulting CQDs. Light metals and alkaline-earth elements can affect ionic strength, pH, and colloidal stability, whereas transition metals may compete with REE ions for oxygen- and nitrogen-containing surface coordination sites or contribute to photoluminescence quenching. Therefore, the material obtained in this work should be regarded as REE-modified CQDs prepared from a real multicomponent waste precursor rather than as CQDs doped with a single, isolated lanthanide ion. Dialysis and filtration remove a fraction of soluble and weakly bound species, but trace impurities may still influence surface chemistry, aggregation behavior, and optical response.

3.2. Visual appearance of CQD dispersions and effect of dialysis

Solutions directly after synthesis exhibited a yellow-brown color under daylight. Organic precursor residues (cherry stones) and REE

precursor residues (fluorescent lamp phosphor) were removed by filtration using filter paper (soft for the final step) and a glass filter funnel. The schematic origin and visual appearance of the samples are presented in Fig. 3.

The obtained samples were coded as follows:

- **Sample A** – carbon nanodots synthesized from cherry stones, before dialysis.
- **Sample B** – retentate after dialysis of sample A.
- **Sample C** – permeate (water) collected after the first dialysis of sample A.
- **Sample D** – carbon nanodots synthesized from cherry stones with the addition of fluorescent lamp powder, before dialysis.
- **Sample E** – retentate after dialysis of sample D.
- **Sample F** – permeate (water) collected after the first dialysis of sample D.

Fig. 3 shows the appearance of the solutions:

- **A–F** – samples under UV light,
- **A'–F′** – the same samples under daylight.

As can be observed in all cases, the fluorescence is notable. However, in the case of a non-dialyzed sample, the intensity of fluorescence seems to be lower. It is probably a combination of several effects. It is well known that CQDs often exhibit pH-dependent fluorescence [26]. This is due, among other things, to the presence of numerous functional groups on the CQD surface [27]. Moreover, in the case of high concentrations of other compounds with high absorption but not fluorescence, an internal filter is formed. This causes only a small volume of the solution to be effectively illuminated by UV radiation. Another reason is that laboratory glass is most often sodium glass, which also partially absorbs UV, thus limiting effective excitation.

Importantly, samples C and F, which are permeates (water) after dialysis, exhibit strong luminescence. This is due to the significant dilution of fluorescent species, being either residual by-products of the synthesis, small enough to pass through the dialysis membrane, or trace amounts of dialyzed solution A and B that entered the permeate through minor micro-leaks in the dialysis setup. This interpretation is supported by the fact that upon high dilution of samples B and E, a similar degree of fluorescence was obtained. Furthermore, permeates collected after subsequent dialysis cycles no longer exhibited any fluorescent properties.

These observations indicate that dialysis affects the apparent optical response mainly by removing low-molecular-weight fluorescent species, residual ions, and weakly bound surface species from the post-reaction

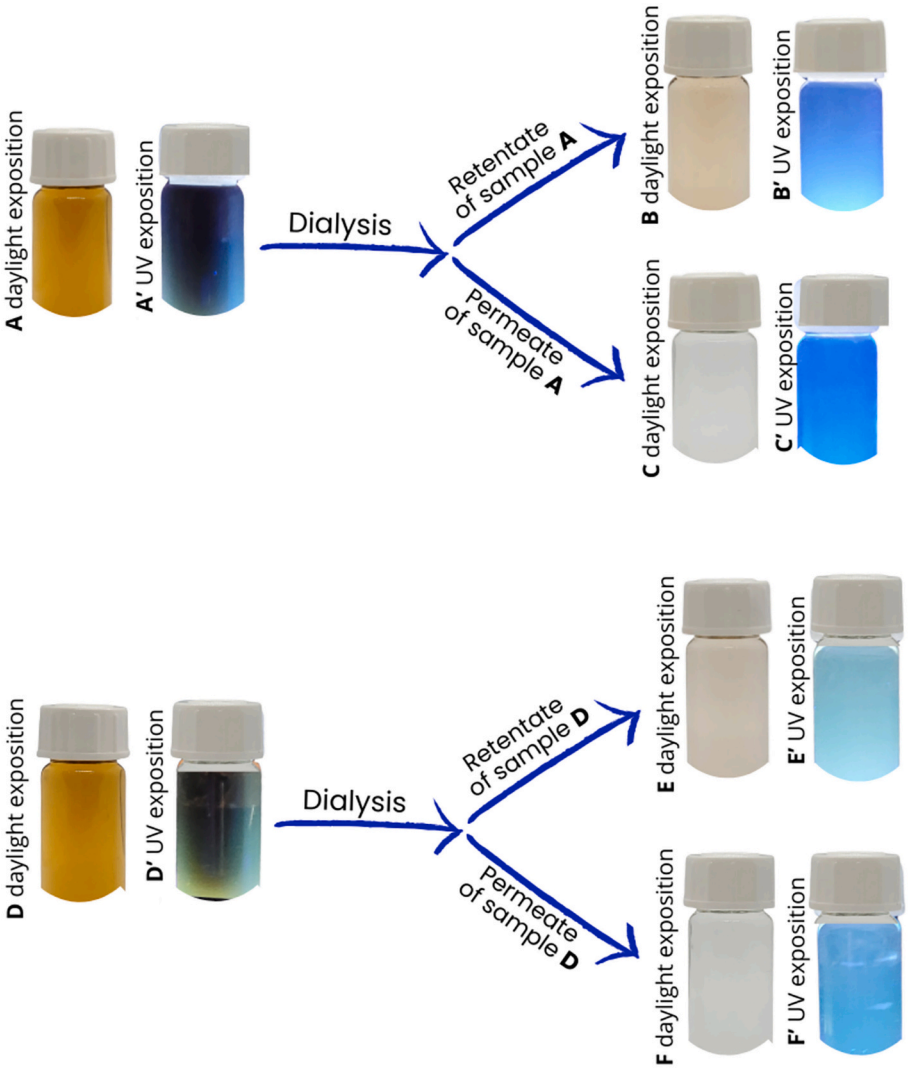

Fig. 3. Origin and appearance of samples A-F under UV light (A-F) and daylight (A'-F'). Samples A–C: carbon nanodots from cherry stones; D–F: carbon nanodots from cherry stones with fluorescent lamp powder; before dialysis (A, D), retentates (B, E), and permeate.

mixture. The as-synthesized solution should therefore be regarded as a complex post-reaction mixture rather than a purified CQD dispersion. Dialysis may also modify pH, ionic strength, and surface protonation equilibria, which can influence PL intensity and the retention/desorption of weakly coordinated REE species. However, such purification is not expected to reconstruct the graphitic/sp^2 carbon core of the CQDs; instead, it primarily affects the surrounding solution chemistry and weakly bound surface functionalities.

3.3. FT-IR analysis of CQDs and REE-modified CQDs

The FT-IR spectra of both undoped CQDs and REE-doped CQDs reveal a series of well-defined absorption bands that map the evolution of surface chemistry upon metal incorporation (see Fig. 4). In the undoped CQDs, a broad O—H stretching band appears at 3431.7 cm^{-1}, indicative of surface hydroxyl groups and adsorbed water engaged in hydrogen bonding [25,28]. The aliphatic $–CH_2–$ vibrations manifest as an asymmetric stretch at 2918.9 cm^{-1} and a slightly lower-intensity symmetric stretch at 2866.0 cm^{-1}, reflecting residual alkyl fragments on the CQD surface [29,30]. These aliphatic functional groups contribute to the chemical reactivity and solubility of CQDs [31]. A strong band at 1629.9 cm^{-1}, present in both, undoped and REE-modified CQDs, is assigned to overlapping graphitic C═C skeletal vibrations with possible contributions from conjugated C═O groups [32–34]. The persistence of this band after REE modification suggests that the conjugated carbon framework is largely preserved, although this band alone cannot be used as definitive evidence for a specific edge-carbonyl structure.

In the fingerprint region, two closely spaced bands at 1428.6 cm^{-1} and 1388.1 cm^{-1} in the pristine CQDs – assigned to symmetric carboxylate ($–COO^-$) stretches [35–37] and $–CH_3–$ bending modes [38], respectively – display a reversal of relative intensity upon REE doping (shifted to ~1432 and ~ 1392 cm^{-1}). This inversion signals preferential coordination of rare-earth ions to surface carboxylate groups, which both stiffens the C—O bond (blue-shift) and enhances its IR activity. The C—O stretching region likewise exhibits a notable red-shift from 1058 cm^{-1} in the undoped CQDs to 1048 cm^{-1} in the doped material, further evidence of metal–oxygen bonding at surface ether, hydroxyl, or carboxylate sites.

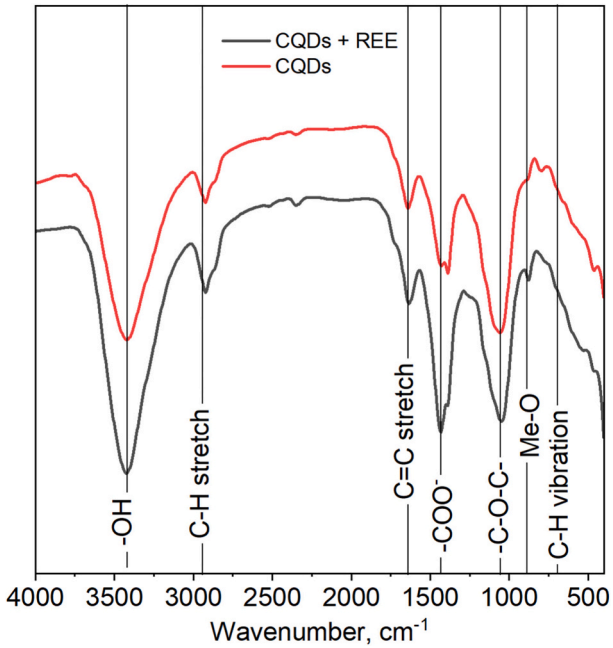

Fig. 4. FT-IR analysis of CQD and REE-doped CQD.

The REE-modified CQD spectrum shows a new band at 877 cm^{-1}, which is absent in the undoped CQDs. This feature should not be assigned to a pure Ln–O stretching vibration, because lanthanide–oxygen stretching modes are generally expected at lower wavenumbers.

The lanthanide-oxygen stretching vibrations are generally found in the lower frequency regions 400–700 cm^{-1} [39]. The most convincing assignment of the 877 cm^{-1} band is to surface CO_3^{2-} (or a mixed Ln-O·COO^- mode) rather than a pure Ln-O stretching vibration. Therefore, the "shift" is due to ligand chemistry and mode coupling (or the presence of carbonates), rather than a simple stiffening of the metal–oxygen bond [39–41]. Conversely, the aromatic C—H out-of-plane bending mode at 798.7 cm^{-1}, prominent in the pristine CQDs, disappears after doping, suggesting that REE coordination perturbs or replaces edge-bound phenolic/aromatic sites. Together, these spectral changes provide a coherent picture of how green-synthesized CQDs are functionalized and stabilized by direct rare-earth metal-oxygen interactions, without disruption of their conjugated carbon core. The peak around 2350 cm^{-1} was not analyzed, as it originates from the hydraulic press oil used during sample preparation and represents a weak artifact.

This type of artifact is commonly observed in FTIR spectra due to contamination from lubricants or oils used in sample preparation. Such peaks are typically weak and narrow, resulting from weak intermolecular interactions, as discussed by Nandiyanto et al. [42].

3.4. Raman analysis

Raman spectroscopy was used to evaluate the structural organization of the carbon framework in CQDs and REE-doped CQDs. In both samples, two broad bands characteristic of carbonaceous nanostructures were observed in the 1000–1800 cm^{-1} region. The D-band envelope is associated with structural disorder, edge defects, and finite-size sp^2 carbon domains, whereas the G band corresponds to the in-plane stretching vibration of sp^2-hybridized carbon atoms.

The spectra were fitted using a minimal two-Gaussian model with a linear baseline. This approach was selected to provide robust comparative descriptors of the CQD carbon framework without introducing model-dependent multi-component deconvolution. The fitted parameters included the D- and G-band positions, their FWHM values, and the ID/IG ratio calculated from the fitted peak heights. The obtained results are shown Fig. 5.

Raman spectra were recorded over a broad spectral range in order to include both the characteristic carbon D/G region and the low-wavenumber region where Ln–O-related vibrations could potentially occur. No distinct Raman bands that could be reliably assigned to Ln–O vibrations were observed in the low-wavenumber region. This point is important because literature data indicate that Raman-active Ln–O-related modes are expected in this spectral range. For hydrated lanthanide(III) ions, symmetric Ln–OH_2 breathing modes have been reported at approximately 343–363 cm^{-1} for light rare-earth aqua ions and at approximately 387–396 cm^{-1} for heavier rare-earth aqua ions [43]. In addition, Raman studies of C-type rare-earth sesquioxides show oxide-related bands in a comparable low-wavenumber region, including features around 338–379 cm^{-1} depending on the rare-earth oxide phase [44]. Therefore, the absence of a well-resolved band in this region indicates that Ln–O vibrations, if present in the REE-doped CQDs, are below the detection limit of the present Raman experiment or are masked by band broadening, the carbonaceous matrix, and sample/substrate-related contributions. Therefore, Raman spectroscopy was not used as direct evidence of lanthanide–oxygen bond formation. Instead, the Raman results support the presence of a defective sp^2-rich carbon framework in both CQDs and REE-doped CQDs. The REE coordination environment is discussed based primarily on FT-IR, XPS, and complementary spectroscopic evidence.

In both spectra, two broad bands characteristic of carbonaceous nanostructures were observed. The band located at approximately 1350–1370 cm^{-1} can be assigned to the D band, which is associated with

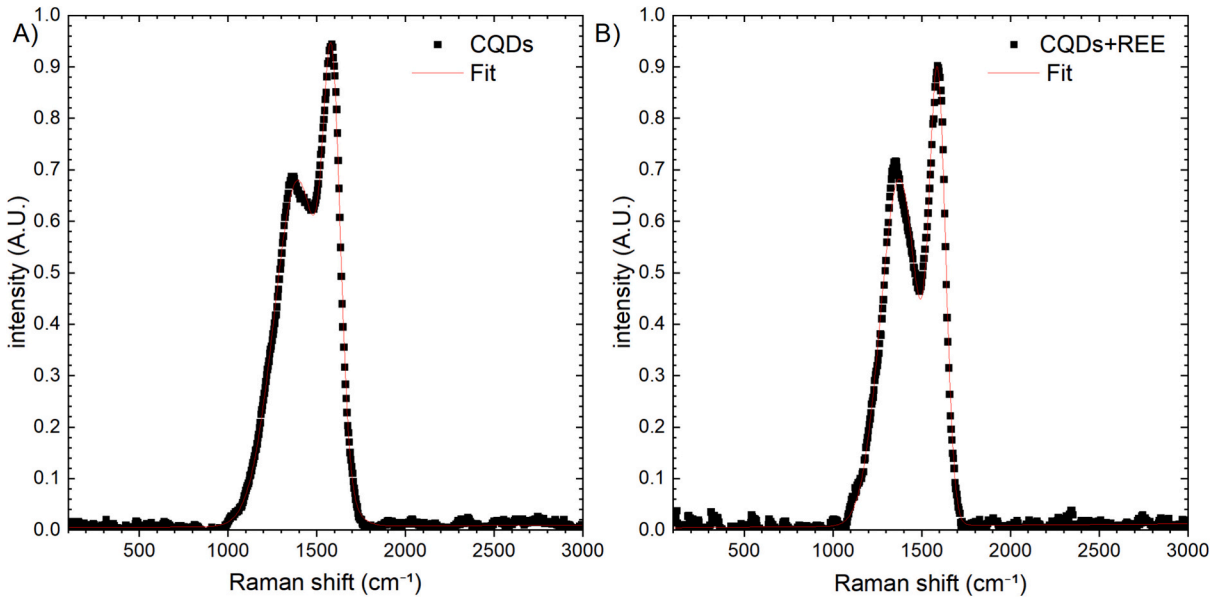

Fig. 5. Raman spectra of CQDs A), and REE-doped CQDs B) deposited on Au substrates and recorded using 532 nm excitation.

structural disorder, edge defects, and finite-size sp^2 carbon domains. The second broad band, observed at approximately 1585–1590 cm^{-1}, corresponds to the G band, arising from the in-plane stretching vibration of sp^2-hybridized carbon atoms.

For the undoped CQDs, the D and G band maxima were located at approximately 1370 and 1585 cm^{-1}, respectively, giving an ID/IG ratio of about 0.75. These values are consistent with literature reports for carbon dots and carbon quantum dots, where the D band is typically observed near 1330–1360 cm^{-1} and is associated with structural disorder, edge defects, surface functionalization, and finite-size sp^2 domains, whereas the G band appears near 1580–1600 cm^{-1} and originates from in-plane stretching vibrations of sp^2-hybridized carbon atoms [45]. For the REE-doped CQDs, the corresponding maxima were observed at approximately 1353 and 1590 cm^{-1}, with an ID/IG ratio of about 0.79. The similar ID/IG ratios indicate that REE incorporation does not substantially disrupt the carbon framework of the CQDs. Instead, both samples retain a disordered sp^2-rich carbon structure typical of carbon quantum dots synthesized from biomass or other carbonaceous precursors [46]. A multi-component deconvolution into additional subbands was not applied because the broad and partially overlapping Raman features of CQDs provide primarily global information on the defective sp^2-rich carbon framework.

3.5. UV–Vis absorption and photoluminescence mechanism

The UV–Vis absorption spectra of both pristine and REE-doped CQD colloids are surprisingly superimposable, indicating that the fundamental electronic structure of the carbon core remains essentially unaltered by rare-earth incorporation. In both samples, a pronounced absorption maximum at 212 nm is observed, which can be attributed to the π–π* transitions of the conjugated C═C bonds within the sp^2-hybridized carbon network of the CQDs (see Fig. 6) [41,47]. This strong UV band is a hallmark of graphitic-like domains and confirms the preservation of the aromatic core in both undoped and doped materials.

Additionally, both spectra exhibit a clear shoulder at ~293 nm, corresponding to n–π* transitions involving surface carbonyl (C═O) or carboxylate groups [48]. The presence of these features in both samples reinforces our FT-IR finding that C═O functionalities are retained and unchanged by REE coordination. After normalization and baseline-matched subtraction, the REE-doped CQDs exhibit a weak additional absorption contribution in the 300–335 nm region, with a residual

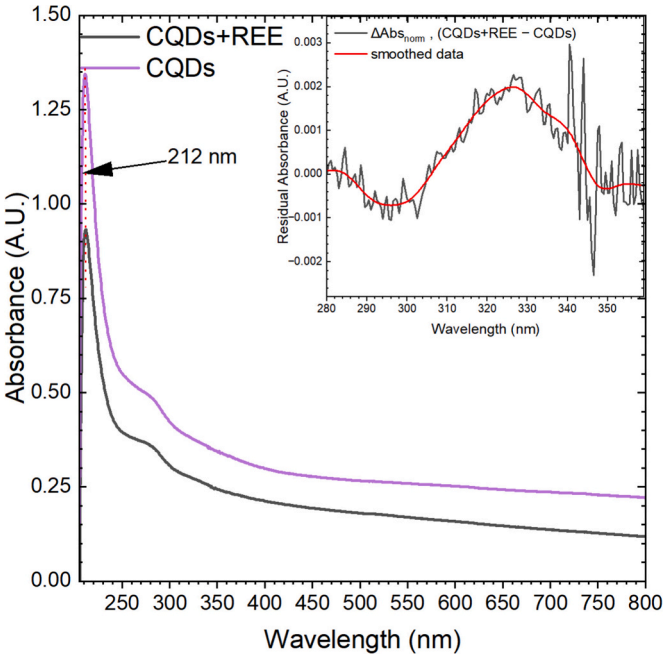

Fig. 6. UV–Vis spectra recorded for CQDs and RRE-doped CQDs.

maximum around 326 nm. This feature is not resolved as a distinct peak in the raw spectrum, but becomes evident in the difference/derivative analysis and is consistent with weak metal–ligand charge-transfer-related states introduced by REE coordination.

This faint absorption may be associated with metal-related surface electronic states or charge-transfer-related transitions involving REE-coordinated oxygen/nitrogen functionalities on the CQD surface [49]. Similar effects have been discussed for metal-doped and lanthanide-modified carbon dots, where metal incorporation can alter surface charge density, introduce additional surface states, and modify UV–Vis/PL responses [50]. The low intensity of the 316 nm shoulder suggests that only a small fraction of the CQD surface participates in such electronic coupling, consistent with sparse and surface-localized REE coordination. This interpretation is consistent with reports on lanthanide-

ion-doped carbon dots, where surface functional groups are described as coordination sites for Ln^{3+} ions and as mediators of energy transfer between the carbon-dot matrix and lanthanide centers [51].

Overall, the near-identical UV–Vis profiles for both samples confirm that rare-earth doping does not disrupt the core π-conjugation of the CQDs, while the subtle emergence of the 316 nm shoulder provides spectroscopic evidence of new metal-related electronic states introduced by REE coordination.

3.6. Fluorescence analysis and quantum yield

The photoluminescence behavior of the obtained CQD colloids (see Fig. 7) exhibits marked evolution both as a function of surface purification (dialysis) and rare-earth doping, underscoring the critical role of surface states and metal coordination in governing emission properties. For the undoped CQDs, excitation-emission matrix scans performed over an excitation range of 200–400 nm with emission registration from 400 to 800 nm reveal that, prior to dialysis, the dominant emissive center is activated at $\lambda_{ex} \approx 398$ nm, yielding a broad emission maximum at $\lambda_{em} \approx 502$ nm. This red-shifted fluorescence likely reflects contributions from small molecular fluorophores and loosely bound surface moieties that are removed or minimized during dialysis. Indeed, following dialysis, the CQDs display a pronounced blue-shift: the excitation optimum moves to $\lambda_{ex} \approx 352$ nm, and the emission peak sharpens and shifts to $\lambda_{em} \approx 440$ nm, consistent with a more homogeneous, defect-dominated emissive core and the elimination of long-wavelength surface trap states. All fluorescence spectra in Fig. 7 have been normalized to a common scale to clearly illustrate differences in emission intensity among the samples. The change in fluorescence intensity of CQDs after dialysis is attributed to the removal of small-molecule species (organic compounds), which alters the local environment of the CQDs and affects the stability of functional groups responsible for emission. The pH change occurring during dialysis, due to the removal of hydrogen ions, also contributes to this effect. For REE-doped CQDs, a similar phenomenon is observed, as surface-adsorbed REE ions partially desorb during dialysis due to changes in concentration and pH, further affecting fluorescence intensity. This behavior is consistent with observations reported in other studies on REE-doped CQDs [52].

For this reason, the observed dialysis-induced spectral changes are interpreted as changes in the population of emissive surface/solution species and surface protonation states, rather than as evidence for reconstruction of the CQD carbon core.

In stark contrast, the REE-doped CQDs exhibit a distinct spectral signature. Before dialysis, the excitation maximum resides at $\lambda_{ex} \approx 374$ nm with emission centered at $\lambda_{em} \approx 460$ nm, indicating that the presence of rare-earth ions creates new intermediate energy levels or surface traps that modulate the fluorescence. After dialysis, the REE-doped CQDs further shift their emission toward the red, with $\lambda_{ex} \approx 397$ nm and $\lambda_{em} \approx 500$ nm. This post-dialysis red-shift and increased emission intensity can be ascribed to stabilized metal–oxygen coordination environments on the CQD surface, which introduce additional radiative pathways – potentially through REE-modified surface states and charge-transfer-related pathways at the CQD/ligand interface – thereby enhancing and tuning the photoluminescent output.

Taken together, these observations demonstrate that (i) dialysis effectively removes extraneous fluorophores and surface traps in undoped CQDs, resulting in blue-shifted, core-dominated emission, and (ii) rare-earth doping imparts new surface-state dynamics that persist even after purification, shifting and broadening the emission profile. Such tunability of both excitation and emission wavelengths via simple post-synthetic treatments and dopant incorporation highlights the versatility of CQDs for tailored optoelectronic applications.

A conceptual energy-level diagram illustrating the proposed photoluminescence pathways in undoped and REE-modified CQDs is shown in

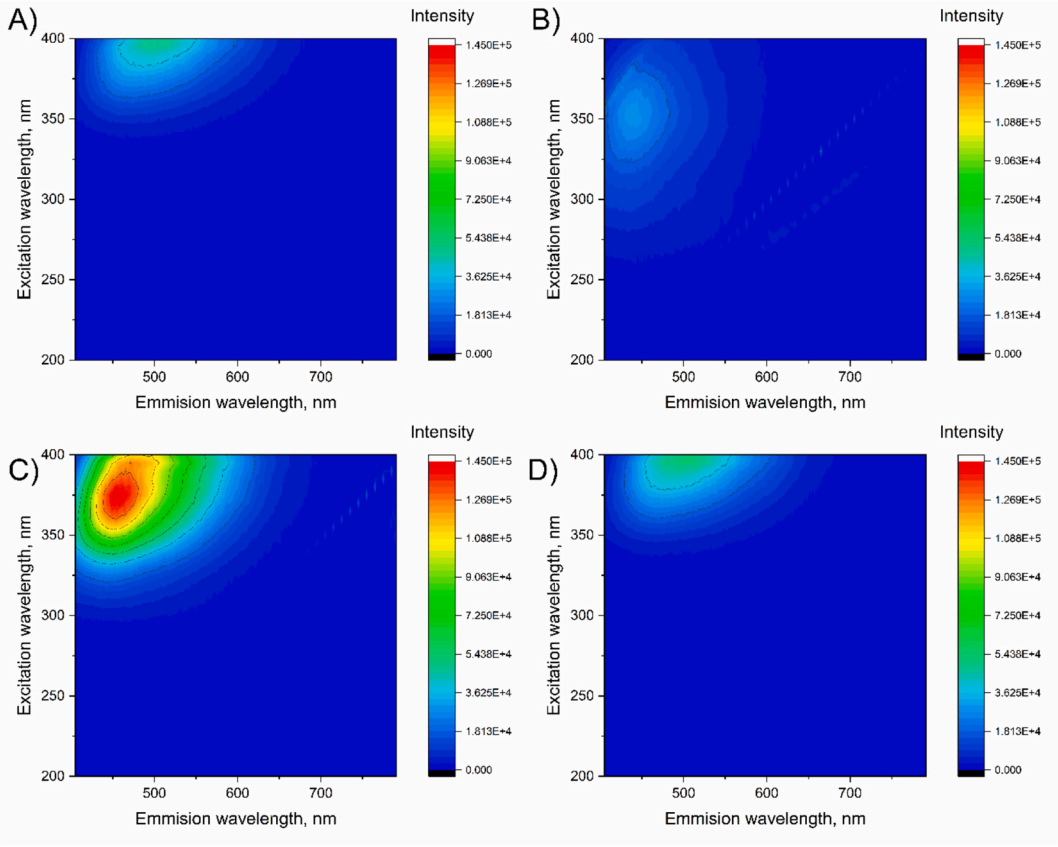

Fig. 7. Fluorescence spectra A) CQDs before dialysis, B) CQDs after dialysis, C) REE-doped CQDs before dialysis, and D) REE-doped CQDs after dialysis.

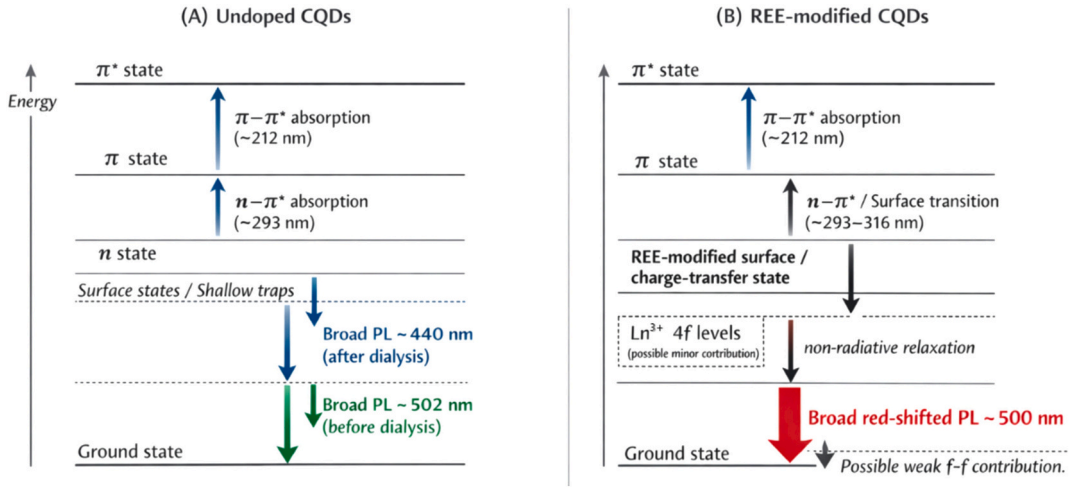

Fig. 8. Conceptual energy-level diagram in CQDs A) undoped, B) REE modified CQDs.

Fig. 8. In undoped CQDs, excitation occurs mainly through π–π* and n–π* transitions, followed by emission from CQD-related surface/core states. Dialysis removes low-molecular-weight emissive species and weakly bound surface/solution species, leading to bluer emission. In REE-modified CQDs, coordination of rare-earth ions to oxygen- and nitrogen-containing surface groups is proposed to generate deeper surface/charge-transfer-related emissive states, resulting in red-shifted broad photoluminescence. Possible lanthanide-centered f–f contributions are shown as secondary and non-dominant.

The PL redshift observed after REE modification is attributed primarily to REE-induced reorganization of surface states and charge-transfer-related emissive pathways rather than to dominant direct lanthanide f–f emission. This interpretation is supported by the broad CQD-like character of the emission bands, whereas purely lanthanide-centered f–f emission would be expected to produce sharper, element-specific transitions. Therefore, the role of REE ions is interpreted mainly as modification of the CQD surface electronic structure through coordination with oxygen- and nitrogen-containing groups, which stabilizes lower-energy emissive states.

The measured QY(%) values for pure CQDs and for REE-doped CQDs are summarized in Table 2.

The PL lifetime values are summarized Table 3. For the calculation of the lifetime with three parameters, we used the following formula for the fitting:

$$y = A + B_1 \bullet e^{-t/\tau_1} + B_2 \bullet e^{-t/\tau_2} + B_3 \bullet e^{-t/\tau_3}$$

where A is the baseline, B_i are the pre-exponentials and τ_i are the individual lifetimes. For the calculation of individual amplitudes (A_i):

$$A_i = B_i \bullet \tau_i$$

and the relative amplitudes A_i (%) are:

$$A_i(\%) = 100 \bullet A_i \Big/ \sum_{i=1}^{n} A_i = 100 \bullet B_i{}^{*}\tau_i \Big/ \sum_{i=1}^{n} B_i \bullet \tau_i$$

It is well-known that CQDs have size-dependent optical properties, which are primarily attributed to quantum confinement (π-π* electronic transitions). When the size of a CQD is comparable to or smaller than the Bohr radius of an exciton, quantum confinement effects become significant. This confinement leads to discrete energy levels, and the energy difference between these levels, and thus the emitted fluorescence wavelength, is inversely proportional to the size of the CQD. The smaller CQDs produced in this work (d ≈ 2–4 nm) are expected to exhibit higher-energy emission (shorter wavelengths) and potentially shorter fluorescence lifetimes because the excited electrons can more easily transition back to the ground state. Electronic transitions involving the surface states (e.g., n-π* transitions from C═O or C—N groups) are often responsible for the longer components of the nanosecond lifetime and can significantly influence the photoluminescence quantum yield and excitation-dependent emission. The interaction between the carbon core and these surface states is also crucial.

PL lifetime measurements were performed at two emission wavelengths. These measurements provide direct evidence of a heterogeneous emissive manifold in CQDs and REE-doped CQDs, in which multiple states core-like and surface/charge-transfer states are populated and selected spectrally. In our data, multiexponential decays are observed at both 455 nm and 520 nm, with the relative weight of the long-lived component increasing at the red detection wavelength, consistent with relaxation into lower-energy surface states. Upon REE doping, the long component remains pronounced and its fractional contribution at 520 nm grows, in line with XAS indications of denser O/N ligand fields and REE–O/N coordination that stabilize deeper radiative traps and produce the observed red-shifted PL. The fact that the

Table 2
QY(%) determination for CQDs and REE-doped CQDs.

Sample name	Excitation wavelength, nm	End of emission, nm	QY, %
CQDs	352	650	1.67
REE-doped CQDs	397	650	2.10

Table 3
PL lifetime values of CQDs and REE-doped CQDs.

CQDs				
Lifetime components	$\lambda_{emission}$ = 455 nm		$\lambda_{emission}$ = 520 nm	
τ_1, ns	1.753 ± 0.053	65.97%	2.090 ± 0.115	42.83%
τ_2, ns	6.435 ± 0.215	14.47%	7.757 ± 0.200	23.92%
τ_3, ns	0.240 ± 0.018	19.56%	0.298 ± 0.015	33.25%
$\tau_{average}$, ns	0.824 ± 0.222		0.740 ± 0.231	
χ^2	0.910		1.179	

REE-doped CQDs				
Lifetime components	$\lambda_{emission}$ = 455 nm		$\lambda_{emission}$ = 520 nm	
τ_1, ns	0.276 ± 0.024	21.82%	0.298 ± 0.021	34.21%
τ_2, ns	1.827 ± 0.046	61.31%	2.236 ± 0.094	42.32%
τ_3, ns	7.369 ± 0.221	16.87%	8.253 ± 0.219	23.47%
$\tau_{average}$, ns	0.871 ± 0.227		0.732 ± 0.240	
χ^2	1.051		1.265	

average lifetime changes modestly while the component distribution shifts with wavelength further supports a model of parallel emissive channels rather than a single-state emitter. Taken together, wavelength-resolved lifetimes, EEM maps, and XAS converge on a common picture: dialysis prunes extrinsic fluorophores and shallow traps (blue-shifting undoped CQDs), whereas REE incorporation re-engineers surface states (enhancing lower-energy emission), all while modest QYs (≈1.5–2%) reflect persistent nonradiative competition in the carbon host. This multi-probe consistency strengthens the assignment of surface-state/charge-transfer–assisted emission as the dominant pathway in the REE-doped CQDs and provides a mechanistic basis for their tunable photophysics.

The relatively low QY values obtained in this work should be interpreted in the context of the deliberately waste-derived and non-optimized synthesis route. The use of real biomass and spent fluorescent-lamp phosphor powder introduces a chemically complex environment, which may increase nonradiative recombination through heterogeneous surface states, residual impurities, and incomplete surface passivation. Therefore, the QY values reported here are not intended to compete with highly optimized CQD systems prepared from purified molecular precursors, but rather to demonstrate that optically active CQDs can be obtained directly from coupled agro-industrial and electronic waste precursors.

3.7. XRD analysis of spent fluorescent-lamp phosphor powder

The XRD pattern of the spent fluorescent-lamp phosphor powder is shown in Fig. 9 together with reference markers for the main crystalline phases assigned according to the literature. The experimental pattern is in good agreement with the XRD pattern reported for end-of-life fluorescent-lamp phosphor residues by Tulay Koc Delice et al. [53], from which the identification of the principal phases was adopted and compared with reference diffraction positions.

Particular attention should be paid to the possible presence of the $BaMgAl_{10}O_{17}:Eu^{2+}$ (BAM) phase (ICSD Card 26–0163), which is one of the main blue-emitting phosphors used in fluorescent lamps [54]. Simulated XRD pattern of $BAM:Eu^{2+}$ reported by Kim et al. also exhibits characteristic reflections in the range of $2\theta \approx 25–40$ deg., with noticeable sensitivity of peak intensities to the Eu^{2+} content [55]. In particular, the relative intensity of reflections around $2\theta \approx 33$ deg. and 36 deg. changes systematically with increasing europium concentration, and a splitting of peaks in the 36–37 deg. region may occur at higher dopant levels. Structurally, BAM crystallizes in a hexagonal β-alumina-type structure (space group P63/mmc), consisting of spinel blocks separated by mirror planes containing Ba^{2+} ions. Europium ions (Eu^{2+}) substitute primarily for Ba^{2+} in these mirror planes, which leads to only subtle changes in lattice parameters but can significantly affect diffraction intensities. As a result, the identification of BAM in complex mixtures is often based not only on peak positions but also on relative intensity patterns. In the analyzed phosphor residue, several reflections in the range of $2\theta \approx 30–40$ deg. may be tentatively attributed to $BAM:Eu^{2+}$; however, their unambiguous identification is complicated by strong overlap with other phases, including Y_2O_3-based phosphors and REE phosphates. Moreover, as indicated in the literature, BAM is typically well-crystallized and produces relatively sharp reflections, whereas the experimental pattern shows significant peak broadening and low signal-to-noise ratio [54]. This suggests that, if present, the BAM phase may occur in a partially degraded or amorphized form, which is consistent with the thermal and chemical treatment of end-of-life fluorescent lamp materials.

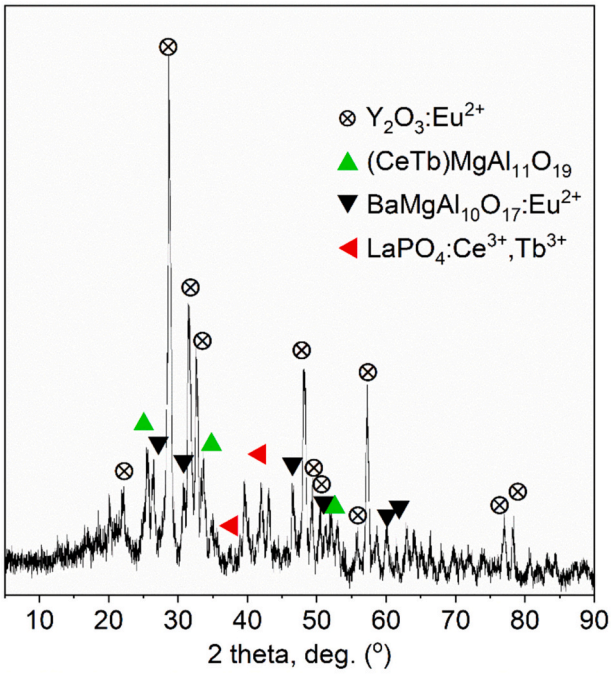

Fig. 9. XRD pattern of spent fluorescent-lamp phosphor powder with reference stick patterns for the main assigned crystalline phases. The principal phase assignment follows the XRD analysis of end-of-life fluorescent-lamp phosphor residues reported by Tulay Koc Delice et al. [53] and was supported by comparison with reference diffraction data.

Another phase that should be considered is $CeMgAl_{11}O_{19}$ (ICSD Card 01–077-1429). It was shown by Yan et al., that $CeMgAl_{11}O_{19}$ exhibits a well-defined diffraction pattern characteristic of magnetoplumbite-type hexaaluminates, with numerous reflections distributed over a wide angular range [56]. Structurally, $CeMgAl_{11}O_{19}$ belongs to the $LnMgAl_{11}O_{19}$ family with a magnetoplumbite-type layered structure, which can be described as alternating $CeAlO_3$ layers and spinel-like $MgAl_{10}O_{16}$ blocks. This structural motif enables extensive cation substitution (Ce^{3+}, Mg^{2+}, Al^{3+}), maintaining crystallographic stability while introducing compositional variability. As reported in the paper, even Ca^{2+} can partially substitute into the structure, which may lead to peak shifts and broadening. From the perspective of phase identification in the studied phosphor residue, this has several important implications. First, due to the large number of reflections and their moderate intensities, $CeMgAl_{11}O_{19}$ may contribute to the "background" of unresolved or weak peaks, especially in the $2\theta \approx 20–60$ deg. region. Second, its diffraction peaks strongly overlap with other aluminate phosphors such as $BaMgAl_{10}O_{17}:Eu^{2+}$, making unambiguous assignment difficult. Therefore, although a definitive identification is not possible based solely on the available XRD data, the presence of $CeMgAl_{11}O_{19}$ is highly plausible in the analyzed material. Its contribution is most likely manifested through a series of overlapping reflections rather than isolated peaks, which may explain part of the unidentified diffraction features observed in the experimental pattern.

It is well known that the dissolution of phosphate salts of REE is significantly difficult, therefore the amount of Ce^{3+}, Tb^{3+}, and La^{3+} were expected to be low. Considering the presence of oxide phases the strongest reflection at ca. 28.7–28.9 deg. can be attributed mainly to cubic terbium oxide phases, particularly Tb_2O_3 (ICSD Card 98–004-0474), with the most intense reflection at 28.8 deg., and or non-stoichiometric TbO (ICSD Card 98–015-9760) of peak maxima shifted toward higher angles. These reflections overlap with contributions from Eu_2O_3 (ICSD Card 98–063-1461), which shows intense peaks at 27.790, 29.445, 30.181, 31.128, 31.298, and 32.106 deg., as well as from mixed Y—Eu oxide (ICSD Card 98–008-4125), with characteristic peaks at 28.074, 29.368, 30.034, 31.003, 31.531 and 32.308 deg.

The broad group of reflections observed between 30 and 33 deg. is therefore assigned to overlapping contributions from Eu_2O_3, $(Y, Eu)_2O_3$, and Tb-containing oxide phases. In particular, the maxima around 31–32 deg. are consistent with Eu_2O_3 reflections at 31.128, 31.298, and 32.106 deg., and with mixed Y—Eu oxide reflections at 31.003, 31.531,

and 32.308 deg.. The feature around 33.3–33.5 deg. can be assigned mainly to Tb-containing cubic oxide phases, including Tb_2O_3 at 33.379 deg., and non-stoichiometric TbO at 33.440 deg..

Reflections in the range of 39–43 deg. may originate from several overlapping REE oxide phases. Eu_2O_3 exhibits peaks at 39.053, 39.597, 40.842, and 42.124 deg., while mixed Y—Eu oxide shows corresponding reflections at 38.925, 39.708, 40.953, and 42.192 deg.. Additional weak contributions from Tb-containing oxides are also possible in this region.

The reflections observed around 46–48 deg. are consistent with Eu_2O_3 and mixed Y—Eu oxide phases. Eu_2O_3 shows a significant reflection at 47.212 deg., while the mixed Y—Eu oxide exhibits an intense reflection at 47.304 deg. These peaks match the experimentally observed broad feature in this region.

Possible CeO_2 contribution cannot be excluded, as CeO_2 (ICSD Card 98–015-5613), exhibits characteristic reflections at 28.062, 32.515, 46.646, and 55.324 deg. However, the position of the most intense experimental peak is closer to the Tb_2O_3/TbO_x reflections than to pure CeO_2, suggesting that CeO_2, if present, is probably a minor or overlapping phase.

In addition to oxide phases, the presence of rare-earth orthophosphates ($REPO_4$) cannot be excluded and is, in fact, highly probable in the investigated material. Fluorescent lamp phosphors are known to contain significant amounts of phosphate-based compounds, which exhibit high chemical stability and resistance to dissolution. Based on the reference diffraction data, phases such as $CePO_4$ (ICSD Card 98–018-2586), $LaPO_4$ (ICSD Card 98–002-1066), and $TbPO_4$ in the xenotime-type structure (ICSD Card 98–002-9316) may be present.

These compounds crystallize in well-defined structures, with $CePO_4$, and $LaPO_4$ of monoclinic monazite-type structure, while $TbPO_4$ crystallizes in a tetragonal xenotime-type structure. Despite structural differences, their diffraction patterns share several characteristic reflections in the range of $2\theta \approx 20$–35 deg., which may overlap with each other as well as with oxide phases, making unambiguous phase identification difficult. The strongest reflections for these phosphates typically occur around $2\theta \approx 26$–31 deg. (monazite-type), and $2\theta \approx 25$–35 deg. (xenotime-type), which coincides with several broad and partially unresolved peaks observed in the obtained experimental pattern.

The occurrence of such phosphate phases is consistent with the known chemistry of end-of-life fluorescent lamp phosphors, where rare-earth elements are commonly incorporated into stable phosphate matrices. This also explains the limited leachability of REEs such as Ce^{3+}, Tb^{3+}, and La^{3+}, as already noted. Furthermore, partial substitution within the $REPO_4$ lattice (e.g., by Dy, Ho, Nd, or Pr) may lead to peak broadening and additional weak reflections, contributing to the large number of unidentified peaks in the experimental XRD pattern.

Those phases contain REE, which can be a source of REE ions to modify the fluorescence of the CQDs [6]. Fluorescent lamps are made from a so-called rare-earth oxide mix. This is dictated by the high cost of separating them before production. Therefore, in practice, all REEs are observed in the composition, with varying mass fractions. The identified phases are most often described in the literature, but as can be seen, a significant portion of the peaks have not been identified. They may likely be associated with other members of the group, such as Dy, Ho, Nd, Pr, etc. Due to the low signal-to-noise ratio, the identification and interpretation of all phases present in the material are challenging.

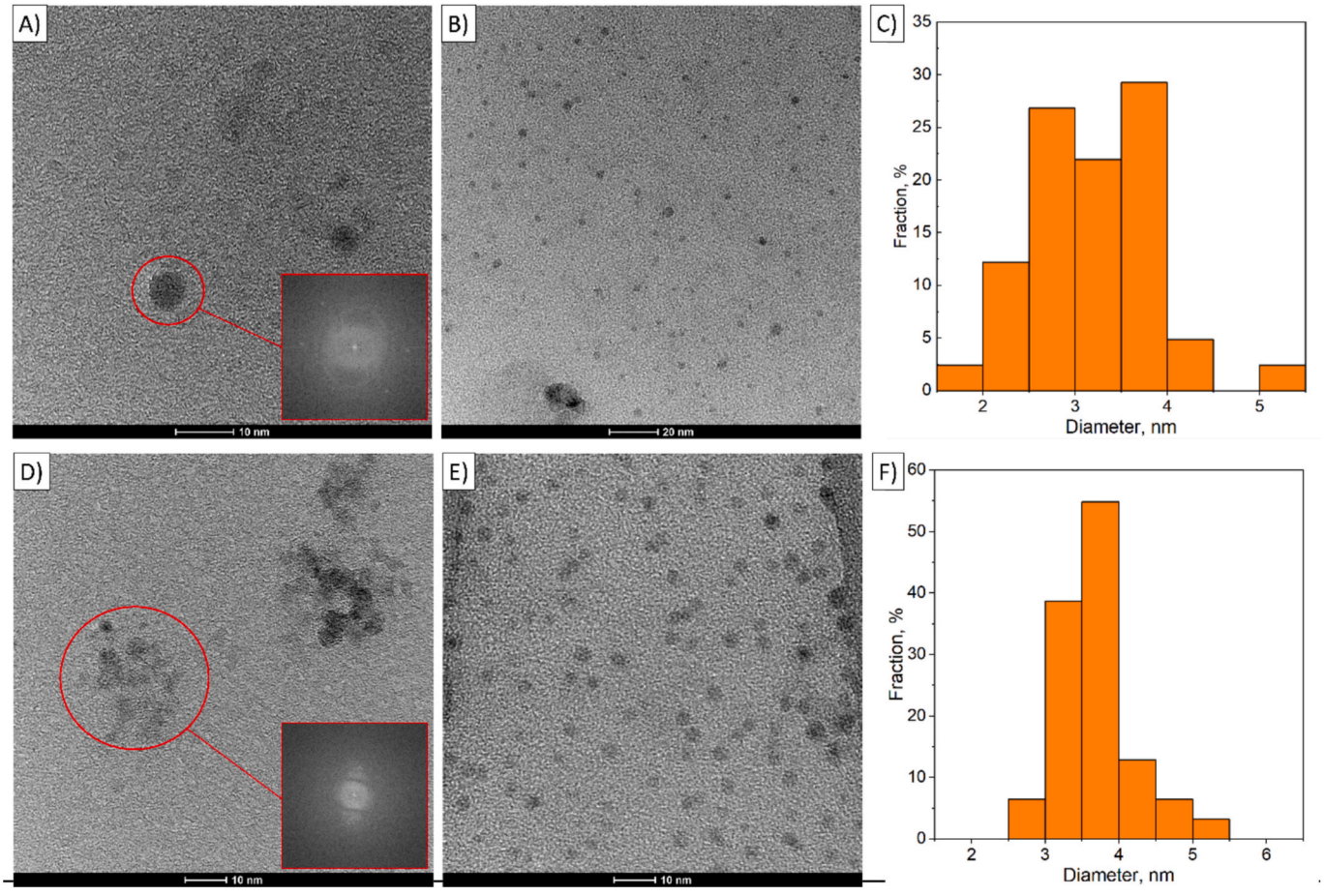

Fig. 10. HR-TEM characterization of CQDs obtained from cherry seeds. (A) Representative HR-TEM image with inset of FFT analysis of a selected sector; (B) selected region at lower magnification; (C) particle size distribution of CQDs based on image B.HR-TEM characterization of REE-doped CQDs obtained from cherry seeds: (D) HR-TEM image with inset of FFT analysis of a selected sector; (E) selected region at lower magnification; (F) particle size distribution of CQDs based on image E.

3.8. HR-TEM analysis, size distribution, and EDX characterization

High-resolution TEM imaging of individual CQDs revealed clear lattice fringes, which were further examined by performing a FFT on a selected particle (Fig. 10). The FFT pattern exhibits four well-defined diffraction spots, each corresponding to an identical interplanar spacing of 0.19 nm. The uniformity of this spacing across all reflections indicates a highly ordered crystalline domain within the CQDs. An interplanar distance of 0.19 nm is characteristic of the (100) lattice plane in graphitic carbon structures, suggesting that the CQDs retain sp^2-hybridized carbon frameworks despite the incorporation of rare-earth dopants. This crystallinity likely contributes to their enhanced optical and magnetic properties.

HR-TEM analysis of the REE-doped CQDs, and in particular the FFT of a single particle, reveals four symmetrically arranged diffraction spots corresponding to an interplanar spacing of 0.24–0.25 nm (see Fig. 10). This spacing closely matches the in-plane lattice constant of graphitic carbon (the (100) reflection, a ≃ 0.246 nm), indicating that the sp^2-hybridized carbon domains in the CQD core retain a well-ordered hexagonal symmetry even after rare-earth incorporation. The presence of four spots in the FFT underscores the preservation of this two-dimensional crystalline ordering.

By contrast, undoped CQDs exhibited FFT spots at 0.19 nm, which we had attributed to more highly curved or defect-rich graphitic facets (e.g., higher-order (101) or edge-related planes). The shift to the larger, in-plane value in the doped sample suggests that REE ions-likely coordinating at surface or edge sites-exert a mild tensile strain on the graphitic lattice, effectively "flattening" or expanding those domains toward the ideal basal-plane geometry.

Crystallinity is enhanced by REE doping, as evidenced by the clear four-spot FFT and the approach to the ideal 0.246 nm in-plane spacing. Lattice expansion occurs upon metal coordination, reflecting the ability of the CQD framework to accommodate REE ions without disrupting the core graphitic network. This structural insight complements our optical and vibrational data, confirming that rare-earth incorporation stabilizes and subtly modifies the CQD lattice while preserving its fundamental sp^2 architecture. Fig. 11 presents the EDX analysis results. The EDX analysis was performed for CQDs doped with REE. In this case, the signal from carbon, oxygen, terbium, silicone, copper, and chloride is observed. It should be underlined that the copper, oxygen and carbon are effects of the substrate. The signal of terbium is directly related to the REE dopant. As shown in Fig. 9, a phase containing terbium is also present in fluorescent lamps. The chloride and silicone are probably residues after incomplete dialysis, or CQDs are surface modified with silica and chlorides.

It should be emphasized that EDX was used here only as qualitative support for the presence of REE-related elements. Quantitative EDX mapping of Dy, Ho, or Nd in individual CQDs is not reliable for the present material because the particles are only a few nanometers in size and the REE content is low and surface-localized. Under such conditions, the generated X-ray signal from a single CQD is very weak and can be strongly affected by the carbon support film, substrate contributions, local aggregation, beam-induced damage, and spectral/background overlap. Therefore, the actual Dy^{3+}/Ho^{3+}/Nd^{3+} loading cannot be robustly determined from EDX mapping in this system. The presence and chemical environment of REE species are instead evaluated using the combined evidence from XPS, EDX, FT-IR, optical spectroscopy, and magnetic-response measurements.

The increased tendency of REE-doped CQDs to aggregate in water, despite their narrower size distribution, can be understood in terms of surface chemistry and colloidal stability. When rare-earth ions bond to oxygen-containing functional groups (–OH, $–COO^-$, –C–O–C–) on the CQD surface, they effectively "block" or consume these hydrophilic sites. This coordination reduces the overall density of free hydroxyl and carboxylate groups that normally hydrogen-bond with water, thereby decreasing the particle's solvation shell and its affinity for the aqueous phase. Moreover, metal binding can neutralize some of the negative surface charge ($–COO^-$) that contributes to electrostatic repulsion between dots. A lower absolute zeta potential weakens the Coulombic barrier against aggregation, allowing van der Waals attractions to dominate. Together, these effects- diminished hydrophilicity and reduced surface charge-lead to a lower energy barrier for particle-particle interactions, and hence, more pronounced clustering in the REE-doped CQD colloids.

Table 4
Apparent mass change of samples.

Sample name	Max. apparent Δm, g
CQD	−0.0012
Dialyzed CQD	−0.0010
Dialysis water CQD	−0.0002
REE-doped CQD	−0.0040
Dialyzed REE-doped CQD	−0.0031
Dialysis water REE-doped CQD	−0.0013
0.025 M Pr(III)	−0.0157

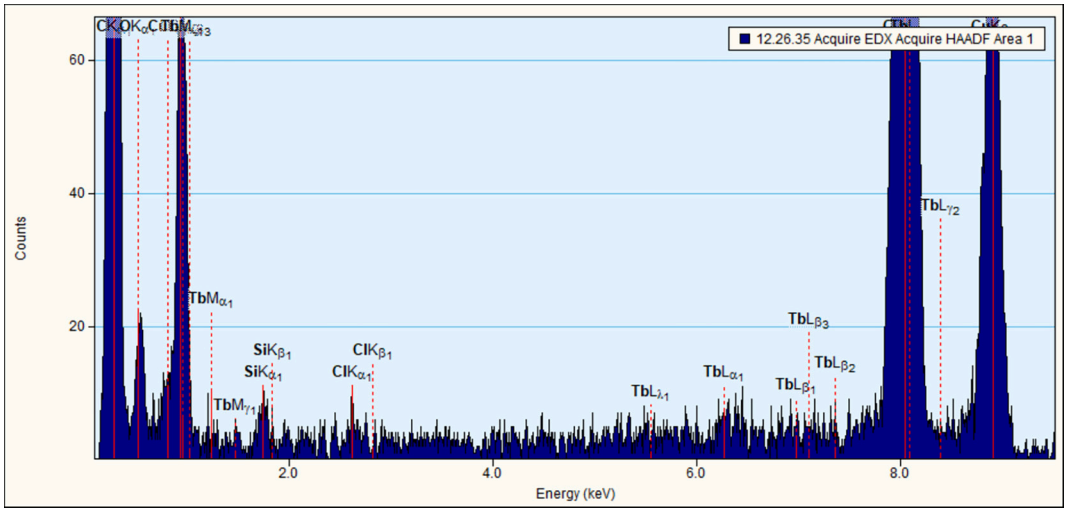

Fig. 11. EDX analysis of CQDs doped with REE.

3.9. Magnetic response of CQDs and REE-modified CQDs

The magnetic-response results are summarized in Table 4 and Fig. 12. REE-modified CQDs exhibited a significantly higher magnetic response than undoped CQDs. The maximum apparent mass change increased from −0.0012 g for undoped CQDs to −0.0040 g for REE-modified CQDs, while the corresponding dialyzed samples showed values of −0.0010 g and − 0.0031 g, respectively.

Table 4 summarizes the magnetic susceptibility measurements obtained for carbon quantum dots synthesized from cherry seeds and their dialyzed solutions, as well as for REE-doped CQDs and their respective dialyzed solutions. For reference, the measurement of a 0.025 M Pr(III) solution was included, since praseodymium is one of the main rare-earth ions present in the phosphor powder recovered from fluorescent lamps and thus represents a realistic dopant species for the synthesized CQDs.

All values presented in Table 4 were corrected for baseline magnetic susceptibility contributions arising from the experimental setup. Specifically, the susceptibility recorded for deionized water and the quartz cuvette used to contain the liquid samples was subtracted from the raw data, ensuring that the reported values represent only the contribution of the investigated nanomaterials and solutions.

As shown in Fig. 12, REE-doped CQDs exhibit significantly higher magnetic susceptibility compared to undoped CQDs. This enhancement can be directly attributed to the intrinsic paramagnetic properties of the incorporated REE ions, confirming that effective doping occurred during the one-step hydrothermal synthesis. The values recorded for dialyzed samples are lower than those obtained before dialysis, which can be explained by the partial passage of magnetic species through the dialysis membrane. Consequently, the first dialysis permeates (samples C and F) display notable magnetic susceptibility despite their strong dilution relative to the original CQD solutions.

Interestingly, the magnetic susceptibility of the first permeates appears relatively high, even though these solutions are strongly diluted. This behavior likely reflects the non-linear nature of susceptibility changes at very low concentrations, where the degree of solvation of paramagnetic species changes markedly upon dilution. In highly diluted systems, the increased number of water molecules per paramagnetic ion alters the effective magnetic response, which could explain the relatively strong susceptibility values recorded for the first permeates. At the same time, permeates collected during subsequent dialysis cycles no longer exhibited measurable magnetic properties, confirming the progressive removal of free paramagnetic species from the system.

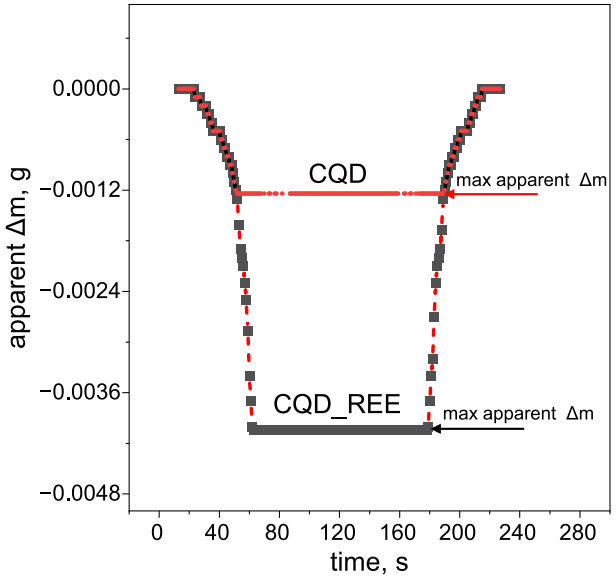

Fig. 12. Apparent mass variations of CQD and CQD + REE solutions over measurement time.

3.10. Chemical-state mapping of CQDs and REE-modified CQDs by XPS

Fig. 13 A-B present survey XP spectra of the pristine CQDs (A) and the REE-doped CQDs (B), respectively. A pronounced difference in elemental composition is evident: the doped sample displays distinct rare-earth features attributable to Ho and Dy, confirming successful incorporation. In addition, both spectra show the presence of nitrogen, fluorine, and sodium (N 1 s ~398–401 eV, F1s ~685 eV, Na 1 s ~1071 eV), which are consistent with elements inherent to the biomass precursor and/or retained from processing. Among these, nitrogen is particularly consequential: N incorporated into the CQD framework strongly modulates the electronic structure, and thus the photoluminescence response, and it also introduces Lewis-basic sites that facilitate coordination to metal ions-hence the N 1 s region is examined in detail in the high-resolution scans. By contrast, the O 1 s envelope in carbonaceous materials does not identify specific compounds i.e., multiple oxygen-containing functional groups (C—O, C═O, O–C=O, hydroxyls) and adventitious adsorbates (H_2O/CO_2) within a narrow binding-energy window (~530–534 eV), causing substantial overlap. Interpretation of this region, therefore, requires careful deconvolution (with consistent constraints and sensitivity factors) and cross-validation against the C 1 s chemistry and, where available, O K-edge XAS. Overall, the survey spectra establish the presence of REE in the doped material and highlight heteroatoms inherited from the precursor, setting the stage for quantitative analysis from the high-resolution regions.

Fig. 14 A-A'A–B show high-resolution XPS C 1 s spectra of the CQDs (A) and the REE-doped CQDs (A'), respectively. In both cases, the envelope was deconvoluted into four chemically meaningful components (A-D), using a Shirley background and mixed Gaussian–Lorentzian peak shapes.

The A component at electron binding energy (BE) of ~284.8 ± 0.1 eV was assigned to C—C bonds in aliphatic chains. The B peak in the BE region of ~286.1–286.4 eV confirmed the presence of alcohol or phenolic (OH) groups at the CQD surface. The carbonyl/quinone groups were indicated by the C component at BE of ~287.7–288.1 eV, and the carboxyl/ester ones were ascribed to the D peak in the BE region of ~288.9–289.3 eV.

A marked decrease in the relative area of the B component (C–OH) is evident upon REE doping, while the C═O (C) and O–C=O (D) contributions persist. This trend indicates that surface hydroxyl groups are consumed or transformed during/after REE incorporation.

Coordination-driven deprotonation: REE^{3+} acts as a strong Lewis acid; C–OH → $C–O^-$ sites bind REE (forming C–O–REE linkages). Such coordination reduces the fraction of neutral –OH detected in C1s and can slightly shift intensity within the C–O/C=O envelope.

From a functional standpoint, depletion of –OH together with persistent C=O/O–C=O moieties suggests a surface enriched with acidic oxygen ligands that are preferred anchoring sites for trivalent REE, which is consistent with the chemical composition of the REE-doped CQDs. This evolution of surface bonding is also in line with the fluorescence behavior discussed elsewhere: stronger metal-oxygen coordination stabilizes lower-energy surface states and contributes to the observed red-shift of photoluminescence. While A component is labeled “aliphatic C–C" for simplicity, in disordered carbon dots, it can include contributions from both sp^3 aliphatic and sp^2 graphitic-like domains.

Fig. 14 B-B′ present high-resolution O 1 s spectra of the pristine CQDs (B) and the REE-doped CQDs (B′). The O 1 s envelope was deconvoluted into four components (A–D) using a Shirley background and constrained Gaussian-Lorentzian shapes.

The A component of O 1 s spectrum at ~531.0–531.8 eV was ascribed to OH– groups at the surface. In the case of the most intensive B peak at BE of ~532.2–533.2 eV, the organic bonding of oxygen to carbon (O—C) was found. This peak can also be related to water adsorption at the analyzed surface. The C spectrum component at ~533.5–535.0 eV

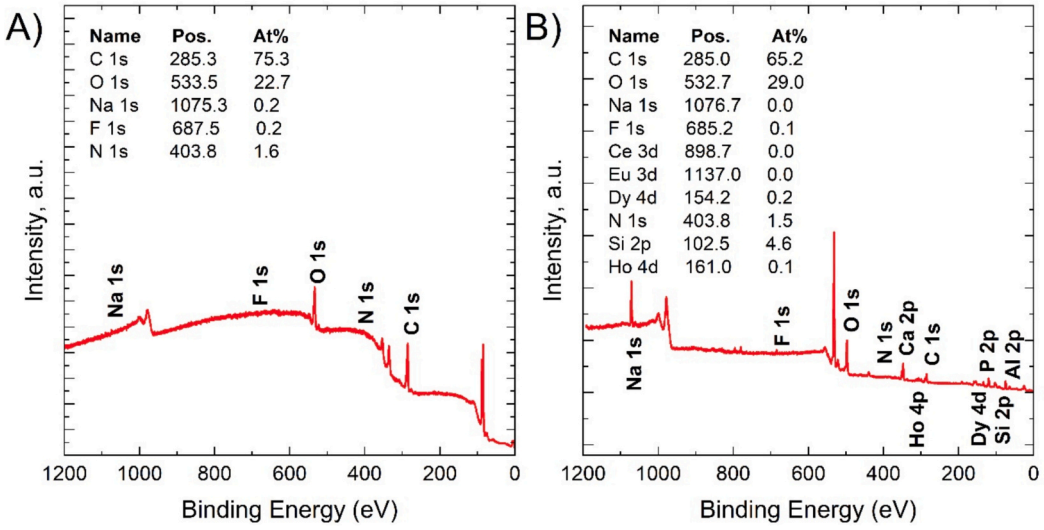

Fig. 13. XPS survey spectra of A) CQDS and B) REE-doped CQDs.

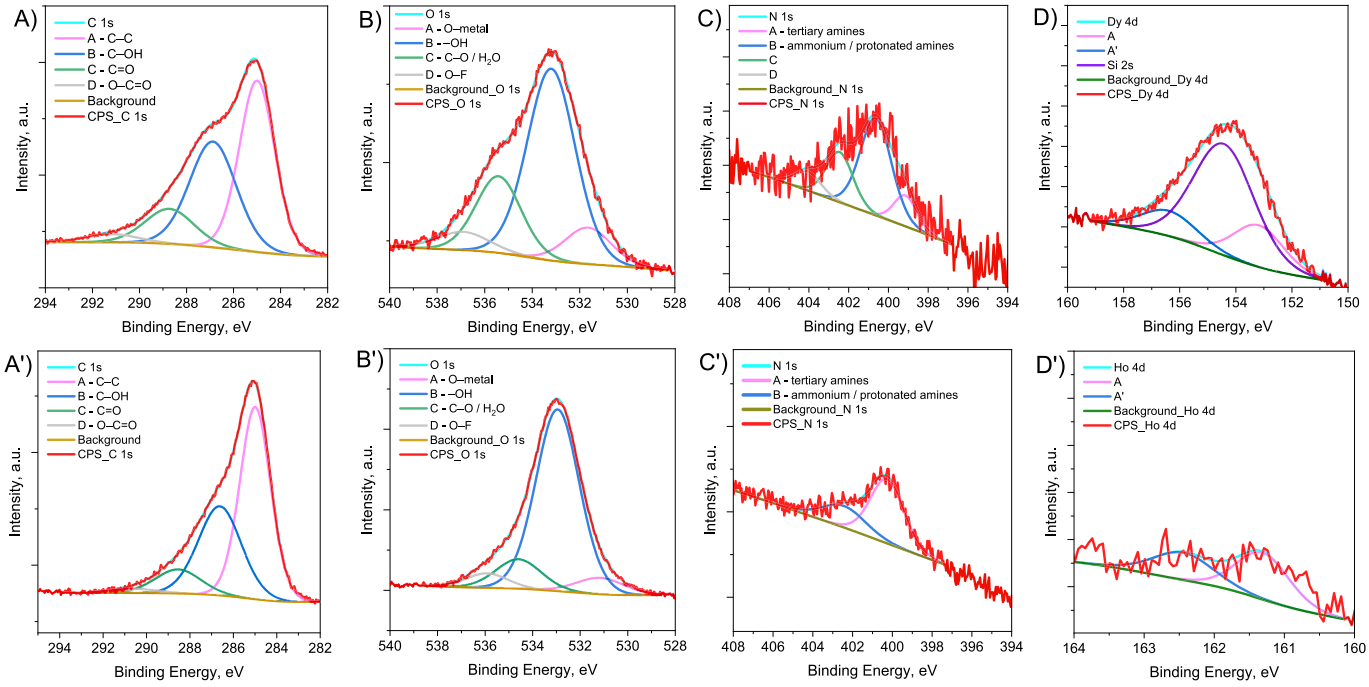

Fig. 14. High resolution spectra for A) C1s for CQDs, A') C1s for REE doped CQDs, B) O 1 s for CQDs, B′) O 1 s for REE doped CQDs, C) N 1 s for CQDs, C′) N 1 s for REE doped CQDs, D) Dy 4d for REE doped CQDs, and D′) Ho 4d for REE doped CQDs.

indicated the presence of double bonds to oxygen (C=O) or a conjugated system of O-C-O bonds. The high BE component of O 1 s spectra (D) can be ascribed to high-BE shake-up/energy-loss tails associated with π* transitions in unsaturated carbon domains.

A pronounced decrease of the A (–OH) and C (C=O) components is observed upon REE doping, whereas component B persists or is redistributed. This is consistent with consumption of surface hydroxyls via (i) coordination-driven deprotonation to form C–O–REE linkages (REE^{3+} as strong Lewis acids) and/or (ii) condensation/oxidative maturation, whereby –OH converts into C═O / O–C=O motifs. The evolution mirrors the C 1 s analysis (loss of C–OH) and aligns with the fluorescence behavior, where stronger REE–O coordination stabilizes lower-energy surface states and shifts emission toward the red.

Fig. 14 C-C′ display high-resolution N 1 s spectra for the pristine CQDs (C) and the REE-doped CQDs (C′).

The N 1 s envelope of the ~~for~~ CQDs sample was deconvoluted into four components (A–D) (see Fig. 14), where A peak at ~398.8–399.6 eV was assigned to secondary amines / nitrile groups (–C ≡ N), This peak captures neutral N—C environments with sp./sp^2 character, including –NH– in secondary amines and nitriles near ~399 eV. The B component at BE of ~400.6–401.2 eV was ascribed to tertiary amines (–NR_3). The ammonium groups or quaternary amines were indicated by the C peak at ~401.8–402.6 eV. The~~n~~ the D component in the BE range of ~405.5–407.0 eV was ascribed to oxidized nitrogen in nitro/nitrite groups (NO_x).

The spectrum shows a clear dominance of amine-type nitrogen (A-C), with only a minor NO_x contribution (D), consistent with nitrogen originating from the biomass precursor and mild post-synthetic conditions.

Upon REE incorporation (see Fig. 14 C), the N 1 s envelope simplifies and was robustly fitted with two components assigned to tertiary amines

(A peak at ~400.7–401.2 eV) or ammonium / protonated amines (–NH_3^+ / –NR_4^+) in case of the B peak at ~402.0–402.8 eV.

The amine signal remains prominent, whereas nitrile (~399 eV) and NO_x (~406–407 eV) bands are not detected within the quantifiable range after doping. This absence can be rationalized by surface complexation and restructuring: (i) inner-sphere coordination of REE^{3+} to Lewis-basic amine sites (and to deprotonated O-donors seen in C 1 s / O 1 s) enhances the relative weight of neutral/tertiary and protonated amines; (ii) nitrile/NO_x groups are either transformed, screened/attenuated by the REE-rich overlayer, or fall below the detection limit under our settings.

The evolution from a four-component pattern (amine + nitrile + minor NO_x) to a two-component amine-dominated spectrum provides a direct spectroscopic indication that N-donor sites mediate REE^{3+} binding on CQD surfaces. The concurrent trends observed in C1s (depletion of C–OH, persistence of C=O/O–C=O) and O 1 s (loss of –OH, growth of O–M / C—O contributions) are consistent with the formation of mixed N/O ligand fields (C–O–REE / N:→REE). Such coordination environments are known to stabilize lower-energy surface states, in line with the red-shifted photoluminescence observed for the REE-doped CQDs.

Fig. 14 D-D′ shows the Dy 4d and Ho 4d core-level XPS regions acquired from the REE-doped CQDs. The clear presence of both dysprosium and holmium is fully consistent with the magnetic measurements reported in Section 3.4 (magnetic properties of the obtained materials), i.e., incorporation of strongly paramagnetic 4f ions into the CQD surface environment.

The Dy 4d envelope was fitted with two components. Interpretation of this region is intrinsically challenging because the Dy 4d manifold exhibits final-state multiplet/charge-transfer structure, and-crucially, in our geometry, overlaps with the Si 2 s line, which adds intensity near the same binding-energy window. As a result, a rigorous oxidation-state assignment from Dy 4d alone is not possible under our conditions. Within the available reference constraints and the oxygen-rich surface chemistry established from C 1 s/O 1 s/N 1 s, the Dy signal is best described as an oxidized Dy species, most plausibly Dy^{3+} coordinated to oxygen donors.

The Ho 4d spectrum exhibits a low signal-to-noise ratio (S/N), reflecting the low surface concentration. Nevertheless, the line shape and binding-energy position are consistent with trivalent holmium (Ho^{3+}) most likely coordinated to oxygen ligands, although coordination to nitrogen (either aminic or oxidized) cannot be excluded.

This assignment is in line with the limited but concordant-reference data (e.g., compendia akin to NIST listings [57]), while we acknowledge that reference coverage for Ho 4d is sparse and the assignment remains provisional.

All REE fits used a common set of constraints (background type, FWHM bounds, energy windows) across samples to ensure comparability. The Si 2 s overlap in the Dy 4d window is the dominant source of uncertainty; it can obscure subtle chemical shifts and satellites critical for precise oxidation-state discrimination. The Ho 4d analysis is limited primarily by counting statistics (S/N). Moreover, the presence of silicon – unambiguously confirmed by EDX measurements further complicates reliable deconvolution of the Dy 4d and Ho 4d bands, since the Si 2 s line (~149.7 eV) lies in close proximity to, and partially overlaps with, the broad and multiplet-structured 4d manifolds of the lanthanides (Dy: main components ~154–158 eV; Ho: ~160–167 eV [58,59]). As a consequence, even minor contributions from the Si signal may mask small chemical shifts and satellite structures that are essential for distinguishing oxidation states and coordination environments. The energy position of the Si 2 s line (~149.7 eV) is well documented in reference databases, while the location and complexity of Dy and Ho 4d states (multiplet and charge-transfer features) are described in detail in the spectroscopic literature, supporting our interpretation of spectral overlap as a significant limitation to confident assignments based solely on the 4d regions.

To strengthen speciation in future work, we recommend separating Si 2 s and REE 4d contributions by: (i) performing parallel analysis of REE 3d/4f regions where applicable, (ii) using silicon-free substrates, (iii) applying longer acquisition times to improve S/N in Ho 4d, and (iv) supporting peak fitting with complementary information from O 1 s, C 1 s, N 1 s, and/or XAS spectra.

Despite spectral congestion (Dy 4d ↔ Si 2 s) and the modest S/N of Ho 4d, the presence of Dy and Ho in the REE-doped CQDs is robustly established, and the oxidized, O-ligated character of these ions is consistent with the high-resolution O 1 s/C 1 s/N 1 s chemistry and with the magnetic response of the materials.

The apparent discrepancy between MP-AES and XPS results arises from the fundamentally different information depths and analytical selectivity of these techniques. XPS is surface-sensitive and probes only the outer few nanometers of the dried CQD surface; therefore, it is particularly sensitive to surface-enriched REE species coordinated to oxygen- and nitrogen-containing functional groups. In contrast, MP-AES quantifies elements present in the bulk leachate or digestion solution and is affected by dilution, detection limits, matrix composition, and possible spectral interferences. Therefore, the two techniques should be regarded as complementary rather than directly comparable. MP-AES describes the solution-accessible composition of the spent fluorescent-lamp phosphor powder, whereas XPS provides evidence of REE-containing species localized at the CQD surface.

This distinction is particularly important for low-abundance REEs, for which a weak or non-detectable MP-AES signal does not necessarily exclude surface-localized species detectable by XPS, and conversely, an element abundant in the leachate is not necessarily efficiently retained at the CQD surface.

3.11. Carbon K-edge XAS analysis

All spectra were exported as two-column ASCII/CSV files (energy vs. TEY signal). When multiple scans were available for the same sample and edge, they were processed identically and then aligned and averaged as described below. For each edge, the signal was corrected by subtracting a linear pre-edge baseline and normalizing to the post-edge level: C K-edge (≈270–345 eV): pre-edge fit over 270–282 eV; post-edge normalization to the mean in 310–330 eV. The obtained results are shown in Fig. 15.

Noise was estimated as the standard deviation in the pre-edge window (σ_pre). Where useful, we displayed difference spectra (CQDs- REE

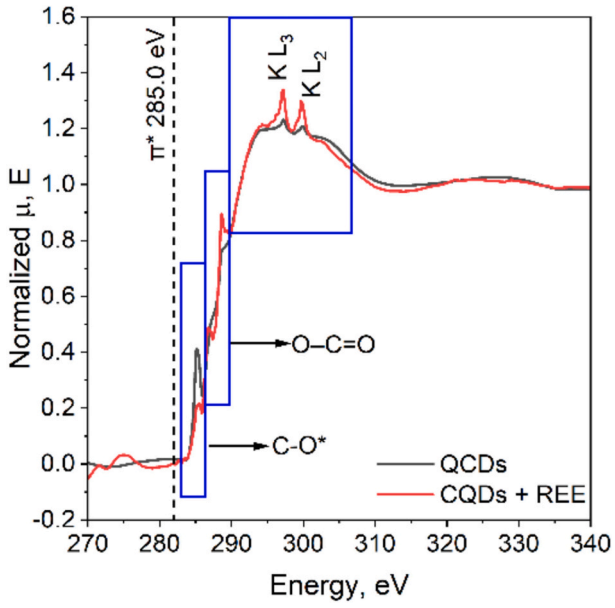

Fig. 15. C K-edge: normalized XAS,

doped CQDs) on the same energy grid, together with a light ±σ_pre band for visual significance. Negative excursions in μ_norm can appear locally as a consequence of baseline subtraction and step normalization; our REE post-edge flattening was applied to minimize such artefacts and to ensure pre-edge ≈ 0 and high-energy post-edge ≈ 1 on both samples.

Measurements addressing the rare-earth component were also performed; however, due to the intrinsically low REE content relative to the carbon matrix, the REE-to-carbon signal ratio was insufficient for reliable quantitative or structural interpretation, and these data are therefore not discussed further. The REE response was evaluated in the $M_{4,5}$ region (~910–1040 eV) using standard pre-edge subtraction and post-edge polynomial normalization, confirming a consistently weak REE signal. This behavior is consistent with a surface-localized modification of the CQDs, with a volumetrically dominant carbon framework and a minor REE contribution confined to the outer surface.

3.12. Integrated interpretation, sustainability aspects, and limitations

Taken together, the structural, spectroscopic, optical, and magnetic results indicate that the one-step waste-based hydrothermal route enables the formation of CQDs whose carbon framework remains largely preserved, while the surface chemistry is modified by REE-containing species originating from the spent fluorescent-lamp phosphor powder. The main functional effects of REE modification are therefore attributed to surface coordination, changes in the distribution of emissive surface states, and the introduction of paramagnetic centers, rather than to bulk reconstruction of the CQD carbon core.

The results of this study demonstrate that a one-step, waste-based hydrothermal route can be used not only to generate carbon quantum dots (CQDs) from agro-industrial waste but also to incorporate rare-earth element (REE) dopants from an electronic-waste-derived precursor in the same reaction vessel. By grinding cherry seeds and spent fluorescent-tube powder together and subjecting the mixture to microwave-assisted hydrothermal conditions in HCl/ethanol media, we achieve simultaneous carbonization, particle formation, and metal coordination without the need for isolated precursor preparation or multistage post-synthesis functionalization. The HCl/ethanol medium was selected to combine two functions: hydrochloric acid promotes the release of REE ions from the spent fluorescent-lamp phosphor powder, whereas ethanol improves the extraction of soluble organic compounds from cherry-seed biomass. This design was intended to favor carbonization of extracted biomass-derived species in solution rather than carbonization occurring only within the solid precursor particles.

Recent studies further illustrate the rapid expansion of sustainable CQD synthesis and application-oriented design. For example, high-yield CQDs have been obtained by solvent-free synthesis from glucose and boric acid, demonstrating that simplified synthetic media can improve the environmental profile of CQD production [60]. In another recent example, waste rubber gloves were converted into fluorescent CQDs suitable for direct ink writing, highlighting the broader potential of waste-derived CQDs for fluorescent patterning and advanced functional materials [61]. In this context, the present work extends the waste-valorization concept by coupling an agro-industrial biomass precursor with an electronic-waste-derived REE source to obtain CQDs with combined optical and magnetic functionality.

The absolute synthesis yield of purified CQDs was not determined in this proof-of-concept study. The post-reaction mixture contains CQDs together with low-molecular-weight fluorophores, soluble biomass-derived organic products, residual acid, salts, free or weakly coordinated REE species, and other components originating from the spent fluorescent-lamp phosphor powder. Therefore, gravimetric drying of the crude product or dialyzed retentate would not provide a reliable yield of pure CQDs. Future work should include standardized purification, separation of molecular fluorophores, determination of the isolated CQD fraction, and optimization of the cherry-seed/phosphor-powder ratio to enable meaningful comparison with other biomass-derived CQD systems.

The term “green synthesis” is used here in the context of precursor selection, process integration, and waste valorization rather than to imply negligible energy input. Hydrothermal carbonization requires elevated temperature and pressure to promote biomass decomposition, dehydration, aromatization, and CQD nucleation. In the present system, these conditions are also important for releasing REE species from the spent fluorescent-lamp phosphor powder and enabling their interaction with the forming CQD surface. Thus, the sustainability rationale of the process arises from the use of low-value waste precursors, the avoidance of purified REE salts, and the integration of carbonization and REE modification into a single reaction step. At the same time, we recognize that energy demand, pressure operation, reagent consumption, and purification losses must be optimized before any scale-up or quantitative environmental assessment can be claimed.

The present work should be considered a proof-of-concept study rather than a complete process-optimization, techno-economic, or life-cycle assessment. Therefore, quantitative claims regarding production cost, synthesis yield at scale, energy demand, or environmental impact would be premature. The synthesis has not yet been optimized with respect to CQD yield, REE incorporation efficiency, reagent consumption, purification losses, or process scale-up. Nevertheless, the route has a clear qualitative environmental rationale: cherry seeds represent an underutilized agro-industrial by-product, while spent fluorescent-lamp phosphor powder is a problematic waste stream containing valuable REEs. The proposed strategy explores the direct conversion of these low-value waste-derived precursors into a functional nanomaterial, avoiding purified REE salts as dopant sources. Its potential economic advantage would therefore not rely on bulk REE recovery alone, which is often limited by low margins, but on transforming waste-derived REE-containing material into higher-added-value CQD-based products. Further work is required to quantify yield, optimize purification, evaluate impurity transfer, assess biosafety, and perform a dedicated techno-economic and life-cycle analysis.

While one-step synthesis of nanodots simultaneously doped with REE ions has been reported in the literature as a strategy for developing dual-function materials for MRI and fluorescent imaging [62,63], the use of spent fluorescent lamp phosphors as an in situ REE source represents a novel approach, aligning with waste valorization trends and enabling the generation of highly functional new materials. This streamlined approach greatly simplifies scale-up and ensures intimate mixing of REE ions with nascent CQD nuclei, promoting efficient surface binding as evidenced by the appearance of Ln–O IR bands and new UV–Vis and photoluminescence features.

FT-IR spectra confirmed the presence of abundant oxygen-containing functional groups (–OH, –COOH, C═O) on the CQDs, which serve both as stabilizers in aqueous suspensions and as coordination sites for REE dopants. The observed shifts in vibrational bands for REE-containing samples indicate direct dopant interaction with the CQD surface chemistry. Complementary XRD analysis of the lamp phosphor precursor confirmed the presence of crystalline rare-earth oxides and phosphates, validating the source of REE species responsible for doping. HR-TEM imaging further revealed well-defined, quasi-spherical nanodots with a narrow size distribution (2–6 nm), where the presence of dopants occasionally introduced local lattice distortions but did not disrupt overall structural homogeneity. Such uniform morphology is critical for the reproducibility of optical and magnetic properties. Similar morphologies were observed for Gd^{3+}-doped carbon dots in “Gadolinium-doped fluorescent carbon quantum dots as MRI contrast agents and fluorescent probes,” with particle sizes ranging from 2 to 8 nm [52], while in “One-pot synthesis of gadolinium-doped carbon quantum dots for high-performance multimodal bioimaging,” particle sizes were reported as 15.0 ± 5.0 nm [62]. Compared to these reports, our CQDs show a narrower size distribution and reduced aggregation, suggesting enhanced structural uniformity that may contribute to more reproducible optical and magnetic behavior.

Perhaps most striking is the three-fold enhancement of magnetic responsiveness observed in the REE-doped CQDs compared to their undoped counterparts. Whereas undoped CQDs exhibit only weak, paramagnetic behavior arising from surface defects, the incorporation of Ce^{3+}/Eu^{3+}/Tb^{3+} (or other lanthanide) centers imparts strong, tunable magnetic moments that remain accessible in aqueous colloids. This magnetic amplification, coupled with the retention of excitation-tunable fluorescence, suggests that the materials may be relevant to future dual-mode imaging concepts. However, at the present stage, this should be regarded only as a materials-level indication of combined optical and magnetic functionality, not as validation of biomedical applicability. Before any bioimaging application can be considered, cytotoxicity, colloidal stability in biologically relevant media, protein-corona formation, biodistribution, clearance, and possible REE ion leakage must be systematically evaluated. The functionality of REE-doped CQDs as a dual-contrast agent has already been evaluated in comparison with commercial agents such as Gadobutrol, in a study where Gd-doped carbon quantum dots were synthesized from glucose via a one-step hydrothermal process [52].

XPS analysis provided direct evidence of successful doping, revealing REE ions stabilized as oxides or coordinated to oxygen-rich surface groups. The chemical-state mapping confirms that doping is surface-mediated and modifies the electronic environment without disrupting the carbon backbone.

The carbon-edge analysis indicates that the CQDs preserve a well-defined carbon framework dominated by sp^2-hybridized domains, accompanied by oxygen-containing surface functionalities. The presence and relative intensity of features associated with these groups suggest that the electronic structure of the carbon core remains largely intact, while surface chemistry plays the primary role in defining the near-edge response. This behavior supports the interpretation that the observed modifications in the CQDs arise predominantly from surface effects rather than from fundamental restructuring of the carbon backbone.

Our comprehensive spectroscopic analysis further reveals that REE incorporation modulates key optical properties of the CQDs. UV–Vis spectra remain largely unchanged in the core π–π* transition at 212 nm and the n–π* shoulder at 293 nm, indicating structural preservation of the graphitic domains, while a new, weak shoulder around 316 nm in doped samples points to metal-to-ligand charge transfer states. In parallel, photoluminescence profiles shift in opposite directions upon dialysis and REE doping: undoped CQDs blue-shift from $\lambda_{em} \approx 502$ nm (pre-dialysis) to 440 nm (post-dialysis), highlighting removal of long-wavelength surface traps, whereas doped CQDs exhibit red-shifted emission (460 nm pre-dialysis to 500 nm post-dialysis) consistent with metal-induced trap states and ligand-to-metal charge transfer pathways. Such tunability in excitation/emission wavelengths underscores the versatility of this one-step platform to tailor optical outputs simply by varying dopant identity and purification protocols. These results are consistent with previous reports on Tb-doped CDs, where REE incorporation also introduced additional absorption shoulders and emission bands characteristic of lanthanide centers (e.g., 490–625 nm for Tb, [62]). In our case, however, the effect manifests primarily as a weak UV–Vis shoulder at 316 nm and a red-shifted photoluminescence profile. While Tb-doped CDs typically display narrow, element-specific f–f transitions superimposed on the broad CD emission, the Gd-doped CDs investigated here exhibit mainly a modulation of the band-edge emission with no distinct lanthanide-related peaks, underscoring that the photoluminescence response is strongly dependent on the REE ion incorporated and the one-step hydrothermal route employed. While the sustainability and functional advantages of this one-step process are clear, safety considerations will be paramount for future development. The use of strong acids and pressurized, high-temperature reactors necessitates careful engineering controls and waste management. Moreover, the fate and toxicity of residual rare-earth ions in biological environments must be rigorously evaluated before any in vivo application. Nevertheless, because the doping occurs concomitantly with nanoparticle formation-avoiding separate ligand-exchange or post-functionalization steps-contaminants and unbound ions can be more readily removed by dialysis or ultrafiltration.

4. Conclusions

In this work, we have demonstrated a sustainable, one-step hydrothermal synthesis of CQDs directly from cherry-seed biomass and spent fluorescent-tube waste, achieving in situ doping with rare-earth elements (REE). The REE-modified CQDs retain the graphitic sp^2 core structure while exhibiting a new FT-IR band at 877 cm^{-1}, assigned cautiously to carbonate-related or mixed REE–O/carboxylate surface modes, together with subtle UV–Vis features around 316 nm that suggest metal-related surface-state contributions. Carbon-edge XAS/EXAFS analysis indicates that the CQDs preserve a stable graphitic carbon framework, with spectral features consistent with a largely intact sp^2 network and surface-localized functional groups rather than bulk structural reconstruction. Raman spectroscopy further supports this interpretation, showing broad D and G bands characteristic of a defective sp^2-rich carbon framework in both undoped and REE-doped CQDs. The comparable ID/IG ratios indicate that REE incorporation does not substantially disturb the carbon framework, suggesting that rare-earth species are mainly associated with surface coordination sites. No distinct low-wavenumber Raman bands attributable to Ln–O vibrations were detected; therefore, Raman spectroscopy was used primarily as a probe of the carbon framework, while evidence for REE incorporation and coordination was derived mainly from XPS, FT-IR, and complementary spectroscopic analysis. Photoluminescence studies reveal dopant-induced red-shifts and charge-transfer pathways, and the doped CQDs display magnetic responsiveness three times greater than undoped analogs. Together, these properties indicate that REE-modified CQDs combine optical and magnetic functionalities that may be relevant to future imaging-related material concepts; however, biomedical applicability cannot be claimed without dedicated cytotoxicity, stability, biodistribution, and REE ion-leakage studies. Beyond their photonic and magnetic performance, the CQDs show a small average size (~3.5 nm), uniform spherical morphology, and surface groups favorable for aqueous dispersibility and potential bioconjugation. The hydrothermal route demonstrates high reproducibility and eliminates the need for external dopant precursors, directly valorizing industrial waste. While safety and biocompatibility assessments remain essential future steps, our streamlined green approach offers a versatile platform for producing multifunctional nanomaterials from waste streams with minimal post-processing.

Future work should focus on improving REE incorporation control, quantifying ion leakage and long-term colloidal stability, optimizing the synthesis yield, and evaluating biosafety before any biomedical application is considered.

CRediT authorship contribution statement

Konrad Wojtaszek: Writing – original draft, Visualization, Validation, Methodology, Investigation, Formal analysis, Data curation, Conceptualization. **Tomasz Michałek:** Investigation. **Katarzyna Skibińska:** Investigation. **Adrianna Pach:** Writing – original draft, Visualization, Investigation. **Krzysztof Pitala:** Validation, Supervision, Methodology, Formal analysis, Data curation. **Krzysztof Mech:** Writing – original draft, Validation, Investigation. **Hossain Aghajani:** Writing – original draft, Methodology, Conceptualization. **Edit Csapó:** Writing – original draft, Validation, Investigation. **Robert P. Socha:** Investigation, Formal analysis, Data curation. **Marek Wojnicki:** Writing – review & editing, Writing – original draft, Visualization, Validation, Supervision, Resources, Methodology, Investigation, Funding acquisition, Formal analysis, Conceptualization.

Declaration of competing interest

The authors declare that they have no known competing financial interests or personal relationships that could have appeared to influence the work reported in this paper.

Acknowledgments

Research at the National Synchrotron Radiation Centre SOLARIS is supported by the Ministry of Science and Higher Education, Poland, under contract no. 1/SOL/2021/2.

We also acknowledge the AGH UST in Krakow from IDUB project No. 6438 for financial support.

This work was supported by the Distinguished Guest Scientists Fellowship Programme (2025) of the Hungarian Academy of Sciences.

Special thanks to Lulu Al Luhaibi for her help and commitment during the Raman measurements, and to all National Synchrotron Radiation Centre SOLARIS staff for support during measurements and data processing.

Data availability

Data will be made available on request.

References

[1] R. Rajesh, D. Kanakadhurga, N. Prabaharan, Electronic waste: A critical assessment on the unimaginable growing pollutant, legislations and environmental impacts, Environmental Challenges 7 (2022) 100507.
[2] N.K. Bhoi, et al., Advancing sustainable electronic waste management: An overview of mechatronics solutions for health, environment, and recycling, Chemosphere 383 (2025) 144501.
[3] L. Peng, Y. Wang, C.-T. Chang, Recycling research on spent fluorescent lamps on the basis of extended producer responsibility in China, J. Air Waste Manage. Assoc. 64 (11) (2014) 1299–1308.
[4] Y.-S. Wu, et al., The Toxicity of Mercury and Its Chemical Compounds: Molecular Mechanisms and Environmental and Human Health Implications: A Comprehensive Review, ACS Omega 9 (5) (2024) 5100–5126.
[5] A.E. Charkiewicz, et al., Mercury exposure and health effects: what do we really know? Int. J. Mol. Sci. 26 (5) (2025) 2326.
[6] Y.-C. Jang, et al., Recycling and material flow analysis of end-of-life fluorescent lamps in South Korea, Energies 15 (23) (2022) 8825.
[7] Jadoun, S., et al., Recovery of Metals from E-waste: Facts, Methods, Challenges, Case Studies, and Sustainable Solutions. Environ. Sci. Technol. Lett., 2025. 12(1): p. 8–24.
[8] E.H. Arruda, et al., Circular economy: A brief literature review (2015–2020), Sustainable Operations and Computers 2 (2021) 79–86.
[9] Jayakumar, A., Carbon quantum dots from natural sources: properties, development, and emerging applications. First edition. ed. 2025, Boca Raton: CRC Press. xiii, 422 pages.
[10] R. Das, R. Bandyopadhyay, P. Pramanik, Carbon quantum dots from natural resource: A review, Mater. Today Chem. 8 (2018) 96–109.
[11] D. Karki, et al., Recent Advances in the Synthesis of Tailored Carbon Quantum Dots and Their Biomedical Applications, ACS Appl. Bio Mater. (10) (2025) 8401–8420, https://doi.org/10.1021/acsabm.5c00491. PMID: 40616519.
[12] H. Shabbir, et al., Eco friendly synthesis of carbon dot by hydrothermal method for metal ions salt identification, Materials 14 (24) (2021) 7604.
[13] R. Guerrero-Gonzalez, et al., Green approach synthesis of carbon quantum dots from agave bagasse and their use to boost seed germination and plant growth, SN Appl. Sci. 5 (8) (2023) 204.
[14] El-Shabasy, R.M., et al., Recent developments in carbon quantum dots: properties, fabrication techniques, and bio-applications. Processes, 2021. 9(2): p. 388.
[15] Gvozdić, V., et al., Sustainable green synthesis of silver nanoparticles using walnut septum waste: characterization and antibacterial properties. Green Process. Synth., 2025. 14(1).
[16] T. Michałek, et al., Recovery of Pd(II) ions from aqueous solutions using activated carbon obtained in a single-stage synthesis from cherry seeds, C 9 (2) (2023) 46.
[17] Y. Dulyanska, et al., Extraction of phenolic compounds from cherry seeds: a preliminary study, Agronomy 12 (5) (2022) 1227.
[18] A. Eštoková, M. Fabianová, M. Radačovský, Life Cycle Assessment and Environmental Impacts of Building Materials: Evaluating Transport-Related Factors, Engineering Proceedings 57 (1) (2023) 5.
[19] H. Shabbir, et al., Understanding the toxicity of carbon dots: the role of synthesis variability, surface chemistry, and biological context, Int. J. Mol. Sci. 27 (9) (2026) 3782.
[20] Y. Zhao, et al., Facile Preparation of Double Rare Earth-Doped Carbon Dots for MRI/CT/FI Multimodal Imaging, ACS Appl. Nano Mater. 1 (6) (2018) 2544–2551.
[21] V. Magesh, A.K. Sundramoorthy, D. Ganapathy, Recent advances on synthesis and potential applications of carbon quantum dots, Front. Mater. 9 (2022).
[22] J.D.G. da Rocha, et al., Exploring the Potential of Rare Earth Doped Carbon Dots: Concepts and Applications, Chem. Eng. J. Adv. 17 (2024) 100583.
[23] Wojtaszek, K., et al., A novel approach for quantifying magnetic susceptibility of aqueous and organic solutions. Chem. Eur. J., 2024. 128(2): p. 488–499.
[24] W. Bulowski, et al., Optimization of gold thin films by DC magnetron sputtering: structure, morphology, and conductivity, Coatings 15 (11) (2025) 1240.
[25] V. Crupi, et al., A FT-IR absorption analysis of vibrational properties of water encaged in NaA zeolites: evidence of a “structure maker” role of zeolitic surface, Eur. Phys. J. E 12 (Suppl. 1) (2003) 47–50.
[26] L.S. Walekar, et al., Selenium and nitrogen co-doped carbon quantum dots as a fluorescent probe for perfluorooctanoic acid, Microchim. Acta 186 (5) (2019) 278.
[27] K. Chang, et al., Synthesis and properties of nitrogen-doped carbon quantum dots using lactic acid as carbon source, Materials 15 (2) (2022) 466.
[28] A.I. Karelin, et al., Water adsorption on tin hydrodioxide and its effect on the contour of the infrared absorption band ν(OH), Russ. J. Inorg. Chem. 58 (5) (2013) 563–569.
[29] L.A. Essa, R.K. Jamal, Studying the structural and optical properties of carbon quantum dots prepared by electro-chemical method, Journal of Optics (India) 53 (2) (2024) 1574–1580.
[30] N.S. Sultan, O.A. Ali, Optical and structural characteristics of carbon quantum dots manufacturing by electrochemical method, Journal of Optics (India) 54 (5) (2024) 3583–3589.
[31] T.H. Huang, et al., Photodynamic antibacterial potential of pomegranate peel-derived carbon quantum dots synthesized via pyrolytic and hydrothermal methods, J. Photochem. Photobiol. A Chem. 469 (2025).
[32] X. He, et al., Efficient Vibrational Energy Transfer through Covalent Bond in Indigo Carmine Revealed by Nonlinear IR Spectroscopy, J. Phys. Chem. B 121 (40) (2017) 9411–9421.
[33] G. Wang, et al., Methylation Mediated Anharmonic Vibrational Signature of Nucleobases: A Case Study of Uracil and Thymine, ChemistrySelect 3 (16) (2018) 4374–4381.
[34] Y. Wu, et al., Intensified C=C Stretching Vibrator and Its Potential Role in Monitoring Ultrafast Energy Transfer in 2D Carbon Material by Nonlinear Vibrational Spectroscopy, J. Phys. Chem. Lett. 10 (6) (2019) 1402–1410.
[35] S. Mitra, et al., CH Mode Mixing Determines the Band Shape of the Carboxylate Symmetric Stretch in Apo-EDTA, Ca2+-EDTA, and Mg2+-EDTA, J. Phys. Chem. A 125 (22) (2021) 4867–4881.
[36] Q.F. Li, et al., A study on interfacial mechanisms and structure of poly(ethylene-co-methacrylic acid)/copper with reflection-absorption infrared spectroscopy, J. Mater. Sci. 41 (24) (2006) 8271–8275.
[37] C.C.R. Sutton, G.V. Franks, G. Da Silva, Modeling the antisymmetric and symmetric stretching vibrational modes of aqueous carboxylate anions, Spectrochimica Acta - Part A: Molecular and Biomolecular Spectroscopy 134 (2015) 535–542.
[38] E. Calabrò, S. Magazù, FTIR Spectroscopy Analysis of Molecular Vibrations in Gasoline Fuel Under 200 mT Static Magnetic Field Highlighted Structural Changes of Hydrocarbons Chains, Pet. Sci. Technol. 33 (19) (2015) 1676–1684.
[39] Y. Jianlin, Y. Yaxian, G. Renao, Raman spectroscopic studies on tropolone complexes with La, Nd, Sm, Yb, Spectrochimica Acta - Part A: Molecular and Biomolecular Spectroscopy 64 (4) (2006) 1072–1076.
[40] M.M. Fernandes, A.C. Scheinost, B. Baeyens, Sorption of trivalent lanthanides and actinides onto montmorillonite: Macroscopic, thermodynamic and structural evidence for ternary hydroxo and carbonato surface complexes on multiple sorption sites, Water Res. 99 (2016) 74–82.
[41] R. Takano, T. Ishida, B. Ay, Synthesis, crystal structure, and luminescence properties of a three-dimensional coordination polymer from europium(iii) carbonate hemioxalate hydrate, CrystEngComm 32 (2022).
[42] A.B.D. Nandiyanto, R. Ragadhita, M. Fiandini, Interpretation of Fourier Transform Infrared Spectra (FTIR): A Practical Approach in the Polymer/Plastic Thermal Decomposition, Indian J. Sci. Technol. 8 (1) (2022) 113–126.
[43] W.W. Rudolph, G. Irmer, On the Hydration of the Rare Earth Ions in Aqueous Solution, J. Solut. Chem. 49 (3) (2020) 316–331.
[44] N. Dilawar, et al., A Raman spectroscopic study of C-type rare earth sesquioxides, Mater. Charact. 59 (4) (2008) 462–467.
[45] R.B. González-González, et al., Synthesis, purification, and characterization of carbon dots from non-activated and activated pyrolytic carbon black, Nanomaterials 12 (3) (2022) 298.
[46] E.A. Diab, M. Ghali, M.M. Mosaad, In vitro antimicrobial and anticancer potentials of green synthesized luminescent carbon quantum dots derived from artichoke leaves, Sci. Rep. 15 (1) (2025) 16199.
[47] E. Dhandapani, et al., Highly green fluorescent carbon quantum dots synthesis via hydrothermal method from fish scale, Mater. Today Proc. 26 (2020) A1–A5.
[48] R. Lestari, I. Kartini, T.D. Wahyuningsih, Effect of Hydrogen Peroxide Concentration to Fluorescence Properties of Carbon Dot from HDPE, Key Eng. Mater. (2022) 106–113.
[49] S. Das, L. Ngashangva, P. Goswami, Carbon Dots: An Emerging Smart Material for Analytical Applications, Micromachines 12 (1) (2021) 84.
[50] Q. Xu, et al., Metal Charge Transfer Doped Carbon Dots with Reversibly Switchable, Ultra-High Quantum Yield Photoluminescence, ACS Appl. Nano Mater. 1 (4) (2018) 1886–1893.
[51] K.F. Kayani, R.F. Hamarawf, Lanthanide ion-doped carbon dots (Ln-CDs) as fluorescent nanoprobes: a review, RSC Adv. 16 (18) (2026) 16631–16652.
[52] M. Wojnicki, et al., Synergistic enhancement of diagnostic imaging: synthesis and preliminary safety evaluation of Gadolinium-doped carbon quantum dots as dual-contrast agent, Molecules 29 (17) (2024) 4075.

[53] T.K. Delice, et al., Impact of extractant type and pH on yttrium recycling from end of life fluorescent lamp, Mater. Proc. 15 (1) (2023) 45.
[54] S. Zhang, et al., Complete recovery of Eu from BaMgAl10O17:Eu2+ by alkaline fusion and its mechanism, RSC Adv. 5 (2) (2015) 1113–1119.
[55] K.-B. Kim, et al., Structural and Optical Properties of BaMgAl10O17:Eu2+ Phosphor, Chem. Mater. 14 (12) (2002) 5045–5052.
[56] X. Yan, et al., Effect of CeMgAl11O19 addition on mechanical and dielectric properties of alumina ceramics for HTCC application, J. Mater. Sci. Mater. Electron. 33 (32) (2022) 24761–24768.
[57] Chase, M.W., NIST-JANAF Thermochemical Tables, 4th Edition. J. Phys. Chem. Ref. Data Monogr., August 1, 1998.
[58] D.J. Morgan, Core-level spectra of metallic lanthanides: Dysprosium (Dy), Surface Science Spectra 30 (2) (2023).
[59] Morgan, D.J., Core-level spectra of metallic lanthanides: holmium (Ho). Surf. Sci. Spectra, 2024. 31(2).
[60] H. Ren, et al., Facile solvent-free synthesis of high-yield carbon quantum dots for hydrogel-mediated fluorescent printing ink, J. Photochem. Photobiol. A Chem. 473 (2026) 116858.
[61] Y. Liao, et al., Transforming waste rubber gloves into value-added fluorescent carbon quantum dots for direct ink writing, J. Environ. Chem. Eng. 13 (2) (2025) 115729.
[62] A. Molkenova, et al., Terbium-doped carbon dots (Tb-CDs) as a novel contrast agent for efficient X-ray attenuation, RSC Adv. 13 (2023) 14974–14979.
[63] Latifi, F., et al., Tb doped carbon dots as a platform for fluorescence ratiometric and colorimetric sensor for deferasirox. Sci. Rep., 2025. 15(1): p. 18075.